UiT
THE ARCTIC
UNIVERSITY
OF NORWAY

Faculty of Science and Technology
Department of Mathematics and Statistics

Modelling the Future of the Arctic Sea Ice Cover

—

Erik Bryhn Myklebust

EOM-3901 Master's Thesis in Energy, Climate and Environment, June 2017

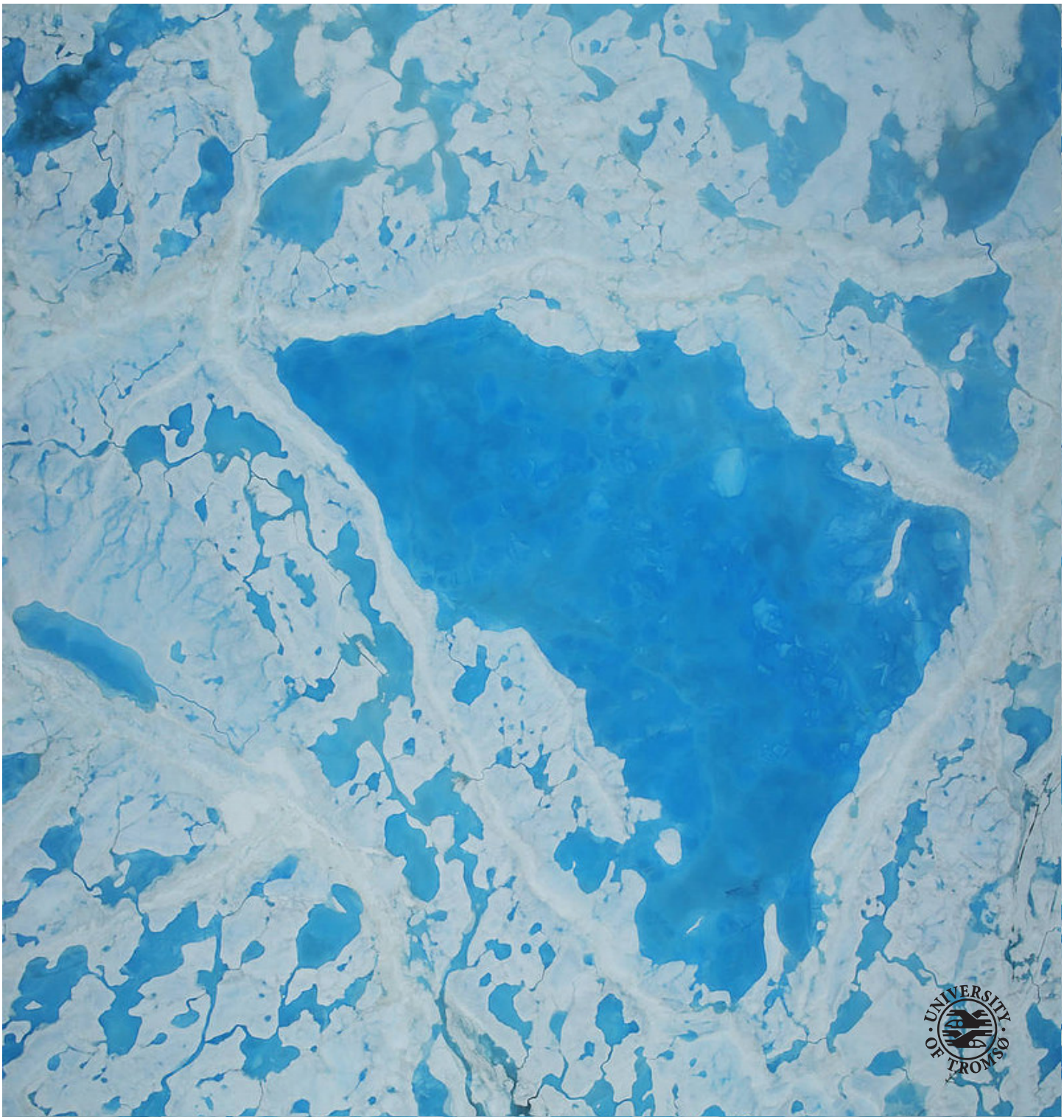

To Mom. Obviously.

“Never half-ass two things. Whole-ass one thing.”
–Ron Swanson (Nick Offerman)

Abstract

Record lows in sea ice cover have recently sparked new interest in the small ice cap instability. The change in albedo when sea ice becomes open water introduces a nonlinearity called the ice-albedo feedback. Forcing a joint energy-balance and sea ice model can lead to unstable ice caps in certain parameter regimes. When the ice caps are unstable, a small perturbation will initiate a tipping point in the sea ice cover. For tipping points in general, a number of studies have pointed out that increasing variance and autocorrelation in time series can be used to predict abrupt transitions, but that the rise in one alone, can cause false alarms. In this study, we will examine these methods, as well as propose new methods that are specific to the problem at hand, and that are more robust when it comes to predicting the abrupt change in sea ice cover. We further investigate the hysteresis that occurs after an abrupt transition and show that the thermal inertia of the deep ocean may delay the recovery of the sea ice cover by several decades in scenarios where pre-industrial CO_2 concentration is restored on century time scale.

Acknowledgements

I would like to thank my supervisor, Martin Rypdal for his ideas and great advice throughout this project. Our discussions have sparked my interest in the field and without your expertise, this thesis would not have been realised.

I would also like to recognise the advocacy of the climate research group at the Department of Mathematics and Statistics. Furthermore, I am grateful to Professor Kristoffer Rypdal for the outstanding course in climate dynamics and help with crucial parts of this project.

I am grateful to all, you know who you are, who have contributed to the project through discussions (no matter the relevance), proofreading, and of course the coffee breaks.

Finally, thanks to my family for endless support throughout my studies.

Contents

Abstract **iii**

Acknowledgements **v**

List of Figures **xi**

List of Tables **xiii**

List of Abbreviations **xv**

1 Introduction **1**

1.1 Tipping Points 3

1.2 Early-Warning Signals 3

1.3 Objective and Significance of Research 4

1.4 Outline 6

2 Background **7**

2.1 Energy Balance Models 7

2.1.1 Linearity of Models 9

2.1.2 Climate Sensitivity 10

2.2 Bifurcation Theory 11

2.3 Early-Warnings Signals 12

2.3.1 Regional Temperatures 13

2.3.2 Ice Cap Thickness 14

3 Models **17**

3.1 North's Model 18
3.1.1 Solar Radiation 19
3.1.2 Outgoing Longwave Radiation 20
3.1.3 Northward Transport 20
3.1.4 Deep Ocean 21
3.2 Wagner and Eisenman's Model 22
3.2.1 Sea Ice Enthalpy 22
3.2.2 Sea Ice Physics 23
3.3 Ice Area and Volume 24
3.4 Default Parameters 25

4 Results **27**
4.1 Fitting the Models 28
4.2 Response to Step Forcing 30
4.3 Early-Warning Signals 32
4.3.1 Monte Carlo Experiments 33
4.3.2 Polar Amplification 36
4.3.3 Thin Ice Cap 36
4.4 Time-Dependent Irreversibility 42

5 Discussion and Analysis **45**
5.1 Modelling 45
5.1.1 Fitting the Models 45
5.1.2 Global vs. Northern Hemisphere 48
5.1.3 Sea Ice and Deep Ocean 48
5.1.4 Climate Sensitivity in Models 49
5.2 Early-Warning Signals 49
5.2.1 Conventional 49
5.2.2 Thin Ice Cap 50
5.3 Time-Dependent Irreversibility 51
5.4 Spatial Model Resolution 52

6 Concluding Remarks **55**

6.1 Summary 55
6.2 Concluding remarks 56
6.3 Further work 56

A Implementation of Models **59**
A.1 Implementation of N81 59
A.2 Implementation of WE15 61
A.2.1 Ghost Layer 61
A.2.2 Freezing Temperature 62
A.2.3 Time-Stepping Scheme 62
A.3 Spatial and Temporal Resolution 64
A.4 Runtime 64

B Calculation of σ^2 and ρ **67**

Bibliography **71**

List of Figures

1.1 Potential wells under anthropogenic forcing. 4

2.1 Energy balance diagram (Reddy et al., 2003) 8
2.2 Climate sensitivity frequency distribution. 11
2.3 Bifurcation diagram 12
2.4 Recovery from perturbation at time t_0. 13

3.1 Model schematic 18
3.2 Co-albedo 20

4.1 Responses to historic forcing. 29
4.2 Normalised global temperature responses to doubling and quadrupling of CO_2. 31
4.3 Ice edge responses to doubling and quadrupling of CO_2. . . . 32
4.4 Variance and autocorrelation of ensemble (200 realizations) pole temperature in N81. 34
4.5 Variance and autocorrelation of ensemble (200 realizations) pole temperature in WE15. 35
4.6 Regional temperature EWS, χ_T. 37
4.7 Normalised annual mean sea ice area and volume from observations. 38
4.8 Normalised annual minimum sea ice area and volume from observations. 39
4.9 Simulated normalised annual mean sea ice area and volume from WE15. 40

4.10 Simulated normalised annual minimum sea ice area and volume from WE15. 40
4.11 χ_I for two different tolerance scenarios. 41
4.12 Ice cap area for the tolerance test. 42
4.13 Irreversibility for slow ramp rate. 43
4.14 Irreversibility for fast ramp rate. 44

A.1 Runtime 65

B.1 Test of convergence for σ^2 and ρ in pole temperature. 69

List of Tables

3.1 Parameter values 26

4.1 Adaption parameters 28

List of Abbreviations

AMO Atlantic meridional overturning circulation

EBM energy balance model

ENSO El Niño Southern Oscillation

ESM earth system model

EWS early-warning signal

GCM general circulation model

IPCC Intergovernmental Panel on Climate Change

MOL method of lines

N81 North's model

ODE ordinary differential equation

OLR outgoing longwave radiation

PDE partial differential equation

SCM single column model

SICI small ice cap instability

TOA top-of-atmosphere

TP tipping point

WE15 Wagner and Eisenman's model

1

Introduction

In the last decade, there has been a dramatic decline in Arctic sea ice cover. Even though Antarctica has not shown the same steady loss of sea ice, there are indications that this could change. 2016 showed a record low in the late-year (October-December) global sea ice extent (Fetterer et al., 2016). The cause is still undetermined. Is this recent change an indication that the ice caps have become unstable?

The nonlinearity associated with the ice-albedo feedback has been studied for its potential to affect the stability of the climate system, and if it can possibly trigger an abrupt transition from a finite ice cap, to perennially ice free conditions. The instability is properly named the small ice cap instability (SICI) (see review North (1984)). This transition is referred to as a tipping point (TP), a term coined by many fields of science, from human behaviour to climate, thanks to the book "The Tipping Point: How Little Things Can Make a Big Difference" by Malcolm Gladwell (2000).

The early studies of potentially irreversible TPs in spatially varying energy

balance models (EBMs) were more concerned with the catastrophic transition to a totally ice-covered Earth, usually called "snowball Earth" (Budyko, 1969, 1972; Held and Suarez, 1974; Sellers, 1969). The snowball Earth bifurcation can be simulated in certain simple general circulation models (GCMs) (Voigt and Abbot, 2012). However, a fully coupled GCM is not able to produce ice at the equator (Poulsen et al., 2001), even though there is evidence that the Earth has been in this state in the Neoproterozoic era (Hoffman et al., 1998).

The SICI in EBMs has been compared to dynamical behaviour in GCMs, where the increase in polar amplification changes linearly up to a annual mean polar temperature of $-5\,^{\circ}\mathrm{C}$ (Winton, 2013). Note that this is way above the loss of the September ice cover, which occurs at about $-9\,^{\circ}\mathrm{C}$. The remaining winter ice cover then exhibits nonlinear behaviour related to the SICI (Bathiany et al., 2016).

In a seasonally varying single column model (SCM) for sea ice there was found behaviour comparable with the SICI (Thorndike, 1992). However, the model used did not describe spatial dependence like the EBM.

Most of our effort is focused on the article by Wagner and Eisenman (2015b), where the objective was to combine the EBM from North et al. (1981)[1] and SCM from Thorndike (1992) into a spatially dependent model with sea ice evolution[2], and investigate at what ratio of diffusion and seasonal variation WE15 has a hysteresis[3] in the sea ice cover. Wagner and Eisenman (2015b) found that it requires a reduction by 70% of either the standard diffusion or seasonality to have a hysteresis wider than $0.2\,\mathrm{W\,m^{-2}}$.

The following subsections give a brief introduction to the concept of TPs and the desirable ability to detect them.

1. Denoting by N81, the model was developed by Budyko (1969); Sellers (1969) independently and summarised by North et al. (1981).
2. Denoting this joint model by WE15.
3. Alternatively irreversibility.

1.1 Tipping Points

A TP is a somewhat vaguely defined concept in climate science. One can define it as the state at which a climate system, small or large, undergoes a transition from one stable state to another. It may be irreversible, like toppling over a glass of wine. By raising the glass back up the wine will not return to the glass. On the other hand, a TP can be reversible, like the tipping over of a seesaw, we can easily tip it back to the previous state by shifting the weight back toward the lighter side.

Climatology TPs include forest dieback, disruption in monsoons, loss of permafrost leading to feedbacks, and polar ice packs (full list of large scale "tipping elements" in Lenton et al. (2008)). We will investigate both reversible and irreversible TPs in this thesis.

1.2 Early-Warning Signals

That a TP occurs may be inevitable, but if we have the possibility to predict it, we would do so. This is our motivation for searching for EWSs. The concept of *critical slowdown* of a dynamical system (Lenton, 2011; Lenton et al., 2008; Scheffer et al., 2009), encompasses the following early-warning signatures:

Slow recovery from perturbations. The potential well becomes shallower and wider in Figure 1.1 and the "ball" can move more slowly, which means more time to return to the stable state.

Increased variance. The width of the well allows larger excursions from the stable state.

Increased autocorrelation. The slow recovery from perturbations can be observed as an increase in autocorrelation.

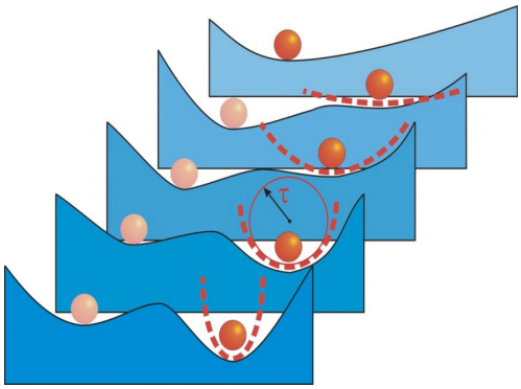

Figure 1.1: Potential wells under anthropogenic forcing.

Figure 2A in Lenton et al. (2008). Potential wells representing stable attractors. Under anthropogenic forcing, we move from dark to light blue. When the right potential well disappears the state of the system, the ball, moves abruptly to new stable state.

Some less used EWSs relating to the stability landscape of the potential wells are

Increased skewness. The system spends more time near the "saddle" (the unstable region between two potential wells), resulting in skewed or even wider probability distribution of the system state.

Flickering. Increased probability of the system spontaneously jumping between two attractors under stochastic forcing. This is closely related to the skewness mentioned above.

We will further expand on these with EWSs of our own in Chapter 2. These new EWSs are specific for the models used in this thesis and are not applicable to all dynamical systems.

1.3 Objective and Significance of Research

The first aim is to add a deep ocean coupling to N81 and WE15, enabling us to conduct the planned experiments involving the extra dynamic this coupling

provides. This brings the models a step closer to a GCM, and can then provide valuable insight into the behaviour of GCMs.

Previously, Wagner and Eisenman (2015a) have shown that it is not possible to detect a rise in variance in sea ice area in WE15 under warming. Later it has been hypothesised that the lower variance is due to the ability of a thinner ice cap to respond faster to forcing (Bathiany et al., 2016). We include N81 in this thesis to gain insight into whether the hypothesis is valid. Since N81 does not include ice enthalpy[4], it should have less variance than WE15.

We will identify previously unidentified EWS for the SICI in both N81 and WE15 (with and without deep ocean coupling) while using conventional and new methods.

WE15 only contains a mixed ocean layer, but our hypothesis is that the hysteresis width will be greatly affected by "heating in the pipeline" in the form of the thermal inertia of a vast deep ocean. If this is true, then representing the deep ocean as a constant heat flux (Wagner and Eisenman, 2015b) is an oversimplification.

Combining these new results should expand our knowledge of the SICI, the prospects of predicting it, and asses the recovery of the sea ice cover in negative emission scenarios.

4. The ice enthalpy is the latent heat of the sea ice which is proportional to the ice thickness.

1.4 Outline

Chapter 2 introduces the concepts of EBM, TP, and EWS in a more precise and technical manner. We will also look at the role of EBMs in climate science in relation to the infinity complex climate system.

Chapter 3 includes the derivations of N81 and WE15. The chapter also justifies the choices for the model parameters.

Chapter 4 first shows how model parameters are fitted to observation data. Second, we present some general results to elucidate issues discussed in Chapter 2. We present the prospect of detecting EWSs for the SICI in this chapter and time-dependent irreversibility (hysteresis[5]) that occurs after the loss of sea ice.

Chapter 5 discusses some of the issues arising when the models are fitted to observed data, then we considers further the impacts of the findings from Chapter 4.

Chapter 6 summarises the findings of the thesis and elaborates further on the implications of these findings and avenues for future work on methods and models.

5. Hysteresis normally refers to the dependence of fixed points (equilibria) on a control parameter like the radiative forcing. This corresponds to the evolution of the actual system state if the parameter variation is infinitely slow. However, the thermal inertia of the deep ocean prevents the system from relaxing to an equilibrium on the time scale of the varied forcing, and hence the observed system path will depend on the rate of change of the control parameter.

2

Background

This chapter aims to give an introduction to the concepts and the methods being applied to the models later on in the thesis. But first, we will introduce the concept of EBMs and why they are useful when studying the infinitely more complex climate system.

2.1 Energy Balance Models

As the name suggests, energy balance is the balance in the Earth's energy budget, i.e., when outgoing radiation is equal to the incoming radiation we are in an equilibrium climate state[1]. Hence when we talk about EBM we strip the complex climate system down to the principle of energy balance. The simplest EBMs depict the change in global temperature simply as the difference in the

1. Here, we mean an *energetic equilibrium* in the form of a fixed point in the energy balance model. The system is of cource not in a thermodynamic equilibrium.

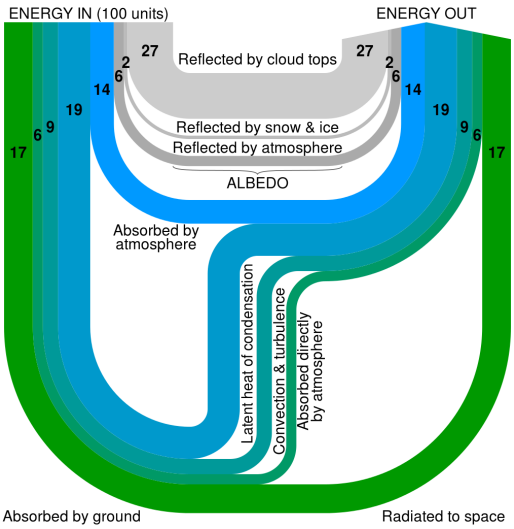

Figure 2.1: Energy balance diagram (Reddy et al., 2003)

incoming and outgoing radiation energy flux;

$$c\frac{\mathrm{d}T}{\mathrm{d}t} = E_{\text{in}} - E_{\text{out}}, \tag{2.1}$$

where c is the heat capacity, which directly relates to the response time of the temperature, T. It is rare that the climate is in a perfect equilibrium all the time, both internal and external forces can create departure from equilibrium. External factors like the Sun's 11-year sunspot cycle will have an effect on the energy into the Earth's climate system. More catastrophic events like big volcanic eruptions can change the climate system drastically, even initiate ice-ages. Modern humans have begun to affect the amount of energy leaving the Earth by the increased greenhouse effect caused by burning of fossil fuels.

The components of E_{in} and E_{out} can be seen in Figure 2.1. However, in an EBM, we combine the bulk of the terms from Figure 2.1 into easier terms. We distinguish between solar incoming radiation and reflected radiation. This means that we can create a term for the energy into an EBM as the product of the proportion of absorbed radiation (co-albedo) and the incoming solar radiation. The remaining outgoing radiation can be found by assuming the Earth is a "grey" body and applying Stefan-Boltzmann law. Both incoming

and outgoing radiation, in terms of the models, will be discussed in detail in Chapter 3.

Earth system models (ESMs) are at the other end of the climate model spectrum, these models include ocean and atmosphere circulation, chemistry, biology, carbon cycle and so on, which enable them to resemble the Earth as closely as possible.

There is also a middle ground called GCM, which parametrizes all the processes that are not interesting for the purpose of the model. If a GCM is used in predicting the weather, it is not important that it includes vegetation or ocean biology, because these things do not affect weather on the time scale we are interested in, particularity the weather next weekend.

But if GCMs and ESMs are superior at representing the Earth's climate than an EBM, so why do we not use them to study TP behaviour?

A model describing present-day weather and climate will not be able to describe ice-age conditions and vice versa, the same goes for models describing the aftermath of global warming, they must differ from present-day models (Rypdal, 2017). So when representing a world different from ours, it is no reason to use models created for present time, instead, we can create EBMs grounded in basic physical processes, which may help us to model and predict TP behaviour.

2.1.1 Linearity of Models

The absorbed incoming radiation into an EBM is dependent on the albedo of the Earth, which is again dependent on the temperature. This fact creates a nonlinear relationship between temperature and reflection, which means that (2.1) is a nonlinear equation. All the models used in this thesis are nonlinear.

In contrast, the global temperature response of most ESMs/GCMs is linear in nature, this is due to the large internal variability in the models which mask the nonlinear ice albedo feedback found in simpler models. These processes include El Niño Southern Oscillation (ENSO), Atlantic meridional overturning circulation (AMO), and other variabilities, on scales from months to decades.

Even though these internal variabilities are "zero-sum games" they mask the effect of nonlinearities such as the ice-albedo feedback. Even in a relatively simple model such as WE15, keeping a slight seasonal solar forcing cycle masks the nonlinear jump to an ice-free Arctic Ocean (Wagner and Eisenman, 2015b).

2.1.2 Climate Sensitivity

Simply explained the climate sensitivity of a climate model is the response to a unit forcing. The temperature response to an instant doubling of pre-industrial CO_2 concentration is alternatively defined as the climate sensitivity of a model.

A collection of climate model responses to doubling of CO_2 is shown in Figure 2.2. The majority of climate models have a response between 2 °C to 4.5 °C with a mean around 3 °C. This results in a climate sensitivity of $\sim 0.8\,\mathrm{K\,W^{-1}\,m^2}$ given that a doubling of CO_2 corresponds to a radiative forcing of $3.7\,\mathrm{W\,m^{-2}}$.

The models used in this thesis are nonlinear and can have different climate sensitivity depending on the forcing scenario. This is presented in Chapter 4.

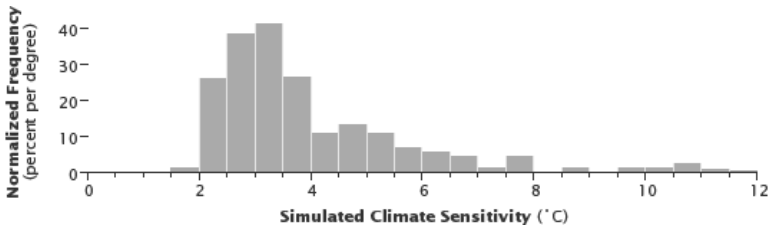

Figure 2.2: Climate sensitivity frequency distribution.

Response to doubling of CO_2 in Intergovernmental Panel on Climate Change (IPCC) climate models. Figure compiled by Lindsey (2010).

2.2 Bifurcation Theory

The dynamical system $\dot{\boldsymbol{T}} = f(\boldsymbol{T}, \boldsymbol{\lambda})$, where $\boldsymbol{T} : t \mapsto \boldsymbol{T}(t) \in \mathbb{R}^n$ and $\boldsymbol{\lambda} \in \mathbb{R}^n$, has equilibrium solutions $\boldsymbol{T}^*$ that we can find by setting $f(\boldsymbol{T}, \boldsymbol{\lambda}) = 0$. Since we only solve for the equilibrium solutions, and we do not know the path of the solutions we have no way of knowing at which equilibrium we are. This is very general, in climate science we usually have an idea of which fixed point we are at. This is trivial by observation, we observe temperature, ocean currents, sea ice area, and so on.

A bifurcation in this dynamical system occurs if smoothly changing parameters $\boldsymbol{\lambda}$ results in the creation, the destruction, or change in stability of fixed points (Kaper and Engler, 2013).

In climate models, we are most interested in observing the stability of the fixed points.

As mentioned, a bifurcation in climate science is often referred to as a TP. TPs can occur if we keep adding radiative forcing to a climate model, which we can see in Figure 2.3. When the ice edge moves northward it will at some point become unstable, and can then transition to the new stable ice-free state given a small perturbation.

Another aspect of this bifurcation is the hysteresis that can arise, that is to say, we cannot simply reduce the radiative forcing and expect the ice to come

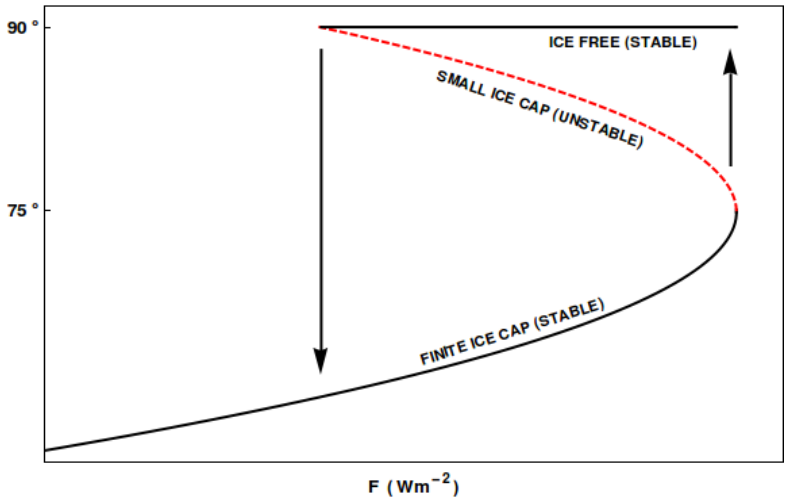

Figure 2.3: Bifurcation diagram

Bifurcation diagram for the SICI. The vertical axis shows the latitude of the ice edge while the horizontal axis indicates the applied forcing. Arrows indicate the hysteresis path. North (1984) finds that the ice cap is unstable for an ice edge north of 75°N.

back at the same point it went away. A large reduction in radiative forcing is required to get a transition back to the stable finite ice cap. N81 and WE15 have a hysteresis width of about 1 W m^{-2} when removing the seasonal cycle (Wagner and Eisenman, 2015b), which corresponds to 56 ppm of CO_2, or the same as the change in CO_2 concentration in the atmosphere from 1970 to present.

2.3 Early-Warnings Signals

As mentioned in Chapter 1, when a dynamical system approaches a TP the system will enter a critical slowdown, which means that a perturbation will have longer recovery time to return to the stable state. This slower recovery is demonstrated in Figure 2.4. And if we keep applying perturbations to a system with long recovery time, eventually the system will jump to a new stable state. This critical slow down is one of the characteristics that we may use as an EWS.

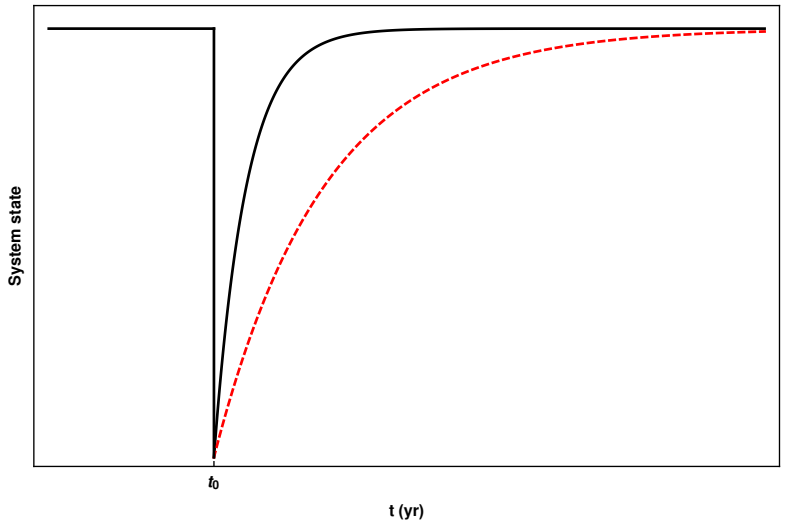

Figure 2.4: Recovery from perturbation at time t_0.

Horizontal axis indicates the system state, e.g. temperature. Vertical axis is time. Solid line returns fast to the stable situation and dashed line represents a system which is close to a TP and has a slow recovery from perturbation.

Conventionally a rise in variance and autocorrelation could imply that the system is going into a critical slowdown. However, the rise one of these quantities alone may create false EWSs for the sea ice area (Wagner and Eisenman, 2015a). We will investigate if there are other methods we can use to detect EWSs in our models.

We will present two alternative EWSs, one of which can be applied to N81 and WE15, the other only apply to WE15.

2.3.1 Regional Temperatures

For a long time, it has been known that the Arctic is warming at a higher pace that the rest of the globe. The pace difference in the regional temperatures may possibly be used as an EWS.

The alternative EWS we define as the change in the polar temperature (above

64°) over the change in global temperature, namely

$$\chi_T = \frac{\Delta T_P}{\Delta T_G}. \tag{2.2}$$

We can substitute the polar temperature with pole temperature to experience a greater amplified effect. However, observation of pole temperatures has a short temporal span and will be more prone to local variability.

2.3.2 Ice Cap Thickness

Efforts have been made to accurately measure sea ice volume, one of them is the PIOMAS project (Schweiger et al., 2011) that employs a combination of satellite data and models to determine the sea ice volume. Schweiger et al. (2011) show that this method has an uncertainty of 1.35×10^3 km^3, which is about one-twentieth of the total ice volume.

One aspect that creates a TP in WE15 is if the ice cap becomes thin, and perturbing a tiny amount may result in that the entire ice-albedo feedback kicks in at once. Searching for this potential EWS we define the quantity;

$$\chi_I = \frac{\text{Area}}{\text{Volume}} = \frac{1}{\text{Thickness}}. \tag{2.3}$$

In Chapter 4 we will investigate how these EWSs, χ_T and χ_I, behave for observed and modelled data.

An EWS is only relevant if we are able to detect it and stop whatever is driving the system to the TP. Hence, we need to explore for which values (2.2) and (2.3) becomes critical. When will it be too late to reverse the process and return to a stable situation? This so-called "point of no return" is established in Chapter 4.

Both of these new EWSs are applicable to a *single* time series, which is how instrumental data are presented. Time series analysis is relevant also when

searching for EWSs in ESMs, since only a few model runs are normally available for analysis. Analysis of ESMs simulations is outside the scope of this thesis.

3

Models

In this chapter, we will derive the two models used to produce the results of this thesis. In both models, we assume an aqua planet (Figure 3.1b) with a fixed mixed layer depth, and deep ocean coupled to this mixed layer. When the temperature becomes low enough in the mixed layer ice will grow. The difference between these two models, N81 and WE15, is related to the ice. WE15 models sea ice evolution including thickness, melting, and freezing. While in N81 the ice only affects the albedo function, i.e., there is no ice enthalpy.

By adding a deep ocean we will be able to increase the climate sensitivity in the models. This is done by moving heat into the deep ocean instead of immediately radiate it to space.

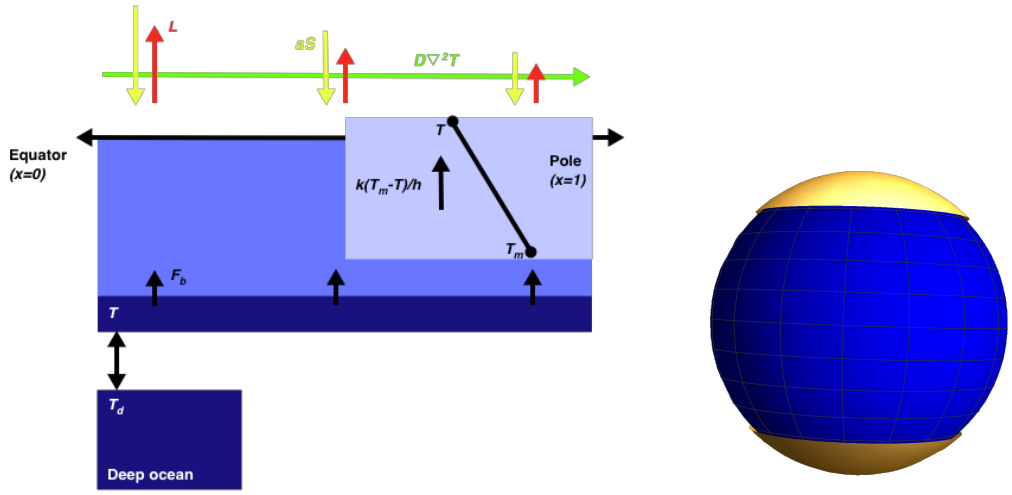

(a) Model schematic **(b)** Aquaplanet

Figure 3.1: Model schematic

(a) Modified model schematic from Wagner and Eisenman (2015b), arrows indicate the components of (3.1)/(3.12). **(b)** Aquaplanet with ice caps.

3.1 North's Model

N81 is described by a single partial differential equation (PDE) (adding deep ocean introduces one more), where the change in temperature is equal to the energy flux into each of the spatial columns from the sun, the deep ocean and neighbouring columns.

$$c_w \frac{\partial T}{\partial t} = -A - BT(t,x) + \alpha(x,x_e)S(t,x) + D\nabla^2 T(t,x) + \kappa(x)(T_d(t) - T(t)) + F(t), \tag{3.1}$$

where $-A - BT$ is the top-of-atmosphere (TOA) outgoing longwave radiation (OLR), αS is the product of the co-albedo and the incoming solar radiation, i.e., the total absorbed energy. $D\nabla^2 T$ is the northward transport of energy. The second to last term is the delay term related to the deep ocean coupling, where T_d is the temperature of the deep ocean. Finally, the last term is any additional radiative forcing, such as anthropogenic forcing. Unlike standard EBM or SCM that do not have a spatially varying temperature, N81 includes both the time evolution (in years) and the spatial dependence of $T = T(t,x)$,

where $x \equiv \sin\theta$ with latitude θ. This implies $x = 0$ at the equator and $x = 1$ at the pole. All figures involving latitude are plotted using x.

3.1.1 Solar Radiation

The total solar forcing is the product of the incoming solar radiation and the co-albedo function.

Following North and Coakley (1979) the incoming solar radiation function is defined as

$$S(t, x) = S_0 - S_1 x \cos(2\pi t) - S_2 x^2, \tag{3.2}$$

where S_0 is the solar radiation at the equator, $x\cos(2\pi t)$ represents the seasonal variation with amplitude S_1, and S_2 is the magnitude of the spatially varying radiation.

Co-albedo is the proportion of incoming radiation that is absorbed and there are many different ways to represent the co-albedo function. Wagner and Eisenman (2015b) use a spatially dependent step function. We will take a different approach, smoothing the step function from Wagner and Eisenman (2015b), that can be interpreted as if we have floating ice sheets or melt ponds.

$$\alpha(x, x_e) = \frac{a_{eq} - a_s x^2 - a_i}{\exp(\gamma(x - x_e)) + 1} + a_i, \tag{3.3}$$

where a_{eq} is the co-albedo at the equator, a_s is the spatially dependent co-albedo and a_i is the co-albedo over the ice. The ice edge, x_e is defined where the temperature changes sign, which differs from North et al. (1981). To achieve the same ice edge in the models this is necessary. This dependence on T introduces the nonlinearity into this model. γ defines the steepness of the function. We will use $\gamma = 150$. Figure 3.2 shows how (3.3) compares to the observed TOA co-albedo. However, we do not fit the parameters in (3.3) to observations.

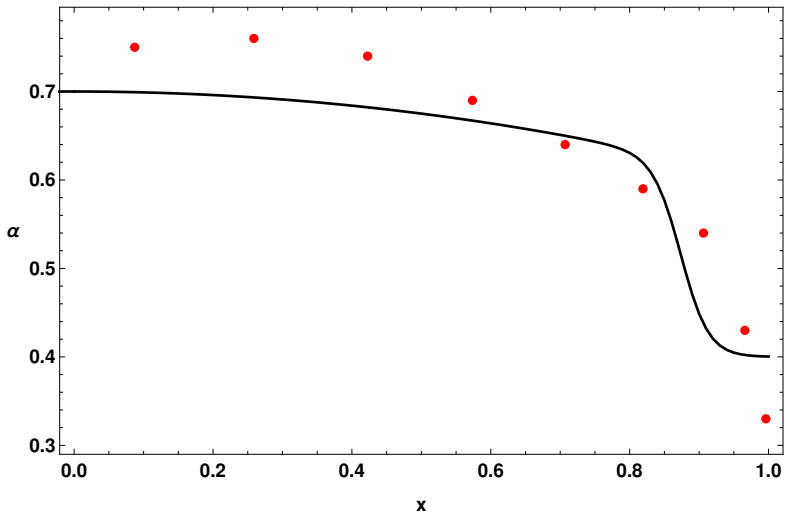

Figure 3.2: Co-albedo

Observed annual mean Northern Hemisphere co-albedo (red dots) from Donohoe and Battisti (2011) and modelled co-albedo from (3.3) (black line).

3.1.2 Outgoing Longwave Radiation

The OLR can be approximated by a linearization of Stefan–Boltzmann law around the pre-industrial temperature (Budyko, 1969);

$$-A - BT, \tag{3.4}$$

where A and B are results of the linearization process. These two constants are obtained by fitting the model to observed data.

3.1.3 Northward Transport

To be able to approximate the transport as a gradient of the surface temperature we must acknowledge that we have a spherical planet where the meridians are converging at the pole. Following North (1975b) (from Legendre's differential equation) the diffusive term will take the form

$$D\nabla^2 T = D\frac{\partial}{\partial x}\left[(1-x^2)\frac{\partial T}{\partial x}\right]. \tag{3.5}$$

Due to the seasonal variations, there will be a small heat transport across the equator where, for simplicity, we restrict ourselves to one hemisphere. This transport across the equator will only change the temperature less than 0.3 K according to Wagner and Eisenman (2015b). The boundary conditions is found by letting the heat content between two latitudes x_1 and x_2 be

$$W_{1,2} = 2\pi \int_{x_1}^{x_2} T \mathrm{d}x. \tag{3.6}$$

If we represent all vertical flux by $R(T, t, x)$ (3.1) takes the form;

$$c_w \frac{\partial T}{\partial t} = R(T, t, x) + D\frac{\partial}{\partial x}\left[(1 - x^2)\frac{\partial T}{\partial x}\right]. \tag{3.7}$$

Integrating both sides of (3.7) over the interval $x \in (x_1, x_2)$ we get a conservation equation for $W_{1,2}$;

$$\frac{c_w}{2\pi}\frac{\mathrm{d}W_{1,2}}{\mathrm{d}x} = \int_{x_1}^{x_2} R(T, t, x)\mathrm{d}x + D(1 - x_2^2)\frac{\partial T}{\partial x}\bigg|_{x_2} - D(1 - x_1^2)\frac{\partial T}{\partial x}\bigg|_{x_1}. \tag{3.8}$$

If the northern boundary is the pole we have $x_2 = 1$ and the flux trough the boundary is zero if $T_x(t, 1)$ is finite. If the southern boundary is the equator we have $x_1 = 0$ and the flux through the boundary is $DT_x(t, 0)$. A zero-flux boundary condition is,

$$T_x(t, 0) = 0. \tag{3.9}$$

3.1.4 Deep Ocean

By adding a deep ocean to the model we add a large thermal inertia that takes a long time to warm up or cool down. This "heating in the pipeline" is the delay effect we are after. A simple PDE which exchanges heat with the mixed layer is

$$c_d \frac{\partial T_d}{\partial t} = \kappa(T - T_d). \tag{3.10}$$

Here c_d is the heat capacity of the deep ocean which is much larger than the heat capacity of the mixed layer. κ is the coupling coefficient between the

mixed layer and the deep ocean. We will set κ as a decreasing logistic function from the equator to the pole, such that we have an ample coupling near the equator and no coupling near the pole. In the real world, the overturning occurs further North, but the primary aim with the deep ocean coupling is to add a larger thermal inertia to the model.

3.2 Wagner and Eisenman's Model

N81 and WE15 are similar, but what WE15 include as well is a sea ice thickness. This thickness makes us able to look more in depth at the mechanisms that create a TP in the sea ice cover.

3.2.1 Sea Ice Enthalpy

To account for the ice thickness we introduce a single column surface enthalpy (Eisenman and Wettlaufer, 2009)

$$E(t,x) \equiv \begin{cases} -L_f h(t,x), & E < 0 \quad \text{(sea ice)} \\ c_w T(t,x), & E \geq 0 \quad \text{(open water)}, \end{cases} \tag{3.11}$$

where L_f is the latent heat of the sea ice, h is the ice thickness, and $c_w T$ is the heat in the open ocean mixed layer (same as in N81).

As for N81, the change in the enthalpy is equal to the sum of the heat fluxes into each column. Either into the ocean mixed layer or the ice from (3.11).

$$\frac{\partial E}{\partial t} = -A - BT + \alpha S + D\nabla^2 T + \kappa(T_d - T) + F_b + F \tag{3.12}$$

(3.12) has the same components as (3.1). Due to the formulation of the model by Wagner and Eisenman (2015b) we need to include F_b which is the steady flow of heat from the deep ocean. This parameter makes sure we get an accurate representation of the sea ice thickness. Discussed further in Chapter 5.

The major difference between the two models is the ice enthalpy and we need to take a look at the physics involved in the evolution of the ice.

3.2.2 Sea Ice Physics

We need to develop a thermodynamic description of the evolution of the sea ice thickness. The heat transport through the sea ice is described by a heat diffusion equation

$$\rho_i c_i \frac{\partial T}{\partial t} = k \frac{\partial^2 T}{\partial z^2} + q, \tag{3.13}$$

where ρ_i, c_i and k are the density, the specific heat, and heat conductivity of the ice, respectively. We assume that they are constant through the ice. q is the heat source arising from penetration of solar radiation into the ice. We can simplify (3.13) by using the four assumptions in Stefan's law (Stefan, 1891)

(i) no thermal inertia,

(ii) no internal heat source ($q = 0$),

(iii) known surface temperature T_0,

(iv) no heat transfer from the water.

Assumptions (i)-(ii) simplifies (3.13) such that there is a linear temperature profile ($\partial T/\partial z$ = constant) through the ice as seen in Figure 3.1a. Assumption (iii) gives the upper boundary condition.

The lower boundary is not fixed but changes when the ice freezes or melts (Leppäranta, 1993)

$$L_f \frac{\partial h}{\partial t} = k \left.\frac{\partial T}{\partial z}\right|_{z=h} - q_w, \; L_f = \rho_i L, \tag{3.14}$$

where h is the ice thickness, q_w is the heat exchange with the mixed layer, and L is the latent heat of freezing. Assumption (iv) and $\partial T/\partial z$ = constant,

reduces (3.14) to

$$L_f \frac{\partial h}{\partial t} = k \frac{T_m - T_0}{h}, \tag{3.15}$$

where T_m is the melting temperature of the sea ice and T_0 is the temperature at the ice surface. By using (3.11) we can see that (3.15) becomes

$$-\frac{\partial E}{\partial t} = k \frac{T_m - T_0}{h}. \tag{3.16}$$

Taking $T_m = 0$ then T_0 will be the temperature that solves (3.12) in the regions covered by sea ice. Inserting (3.16) into (3.12), we get

$$\frac{kT_0}{h} = aS - A - BT_0 + D\nabla^2 T_0 + F. \tag{3.17}$$

Due to assumption (iv), there is no heat transferred to or from the deep ocean in the ice-covered regions, i.e., $\kappa = 0$ and $F_b = 0$. This results in two regions for ice, freezing and melting. Using (3.17) together with (3.11) for open water, the surface temperature is[1]

$$T = \begin{cases} E/c_w, & E > 0 \qquad \text{(open water)}, \\ 0, & E < 0,\ T_0 > 0 \ \text{(melting ice)}, \\ T_0, & E < 0,\ T_0 < 0 \ \text{(freezing ice)}. \end{cases} \tag{3.18}$$

Thus the governing equations for WE15 are (3.12), (3.17), and (3.18).

3.3 Ice Area and Volume

We will look at both the ice area and volumes response to climate forcing and therefore we need to define these quantities. Define the relative ice area as

$$A(t) = 1 - x_e(t) \tag{3.19}$$

1. T_0, by definition, is the solution to (3.17). If $T_0 > 0$ it does not represent the surface temperature, which is zero degrees Celsius in the case of melting ice.

where $x_e(t)$ is the ice edge at any time t.

It has been pointed out in Wagner and Eisenman (2015a) that ice volume may be a better quantity to observe when it comes to predicting a TP. Since WE15 contains ice thickness this can be done. Volume is defined as the integral of the ice thickness over the hemisphere of radius r;

$$\begin{aligned} V(t) &= 2\pi \int_{\theta_e}^{\pi} r\cos(\theta)\, h(t,\theta) r \,\mathrm{d}\theta \\ &\overset{x=\sin(\theta)}{=} 2\pi \int_{x_e}^{1} r^2 h(t,x)\mathrm{d}x \end{aligned} \tag{3.20}$$

where $h(t,x)$ is the ice thickness from (3.12). (3.20) is computed as a sum.

3.4 Default Parameters

The range of parameters in the models is broad. We will try to justify the choices for the default parameter values.

Table 3.1 contains all default parameter values and a short description of each. The diffusivity, D varies in the literature from 0.4 (Lin and North, 1990) to 0.66 (Rose and Marshall, 2009). We chose the same diffusivity as Wagner and Eisenman (2015b). Due to the method used to add a deep ocean to the models, the diffusivity is slightly different in these models, to ensure the same ice edge. This is shown in Chapter 4.

The insolation at the equator, S_0, and the spatially varying insolation, S_2, can be found by Legendre polynomial coefficients, using the ones found by North and Coakley (1979). The seasonal varying insolation, S_1, is set larger (25% as Wagner and Eisenman (2015b)) than in North and Coakley (1979) to represent the present climate properly, especially the sea ice thickness. S_1 is also one of the parameters we will change to create an unstable climate. The co-albedo coefficients are adopted from North (1975b). a_{eq} and a_{sp} are a result of analysis of the albedo distribution from Sellers (1969). a_i is the proportion of absorbed

Symbol	Description	Default value
D	Default diffusivity ($\mathrm{W\,m^{-2}\,K^{-1}}$)	0.6
A	OLR at $T = 0$ ($\mathrm{W\,m^{-2}}$)	Model dependent
B	OLR temperature dependence ($\mathrm{W\,m^{-2}\,K^{-1}}$)	Model dependent
c_w	Mixed layer heat capacity ($\mathrm{W\,yr\,m^{-2}\,K^{-1}}$)	7.3
c_d	Deep ocean heat capacity ($\mathrm{W\,yr\,m^{-2}\,K^{-1}}$)	106
S_0	Insolation at equator. ($\mathrm{W\,m^{-2}}$)	420
S_1	Default insolation seasonal dependence	338
S_2	Insolation spatial dependence	240
a_{eq}	Ice-free co-albedo equator	0.7
a_{sp}	Ice-free co-albedo spatial dependence	0.1
a_i	Sea ice co-albedo	0.4
k	Sea ice thermal conductivity ($\mathrm{W\,m^{-2}\,K^{-1}}$)	2
L_f	Sea ice latent heat of fusion ($\mathrm{W\,yr\,m^{-3}}$)	9.5
$\bar{\kappa}$	Deep ocean coupling, spatial mean ($\mathrm{W\,m^{-2}\,K^{-1}}$)	0.73
F	Radiative forcing ($\mathrm{W\,m^{-2}}$)	varies

Table 3.1: Parameter values

radiation over ice and snow. We use the values corresponding to pure ice (frozen water with no impurities) with density $\sim 900\,\mathrm{kg\,m^{-3}}$ for the thermal conductivity k and the latent heat L_f (Wagner and Eisenman, 2015b).

The heat capacities for both the mixed layer and the deep ocean are adapted from Geoffroy et al. (2013), where they fit a two-box model to the abrupt $4 \times CO_2$ and 1% increase CO_2 per year CMIP5 experiments. Since we have a spatially dependent deep ocean, we only adopt the mean of the coupling coefficient, κ from Geoffroy et al. (2013).

The OLR parameters A and B are crucial for finding the best fit for the models to observed temperature, we will find these parameters in Chapter 4.

The numerical integration of both N81 and WE15 is shown in Appendix A.

4

Results

First, we consider fitting the models to observed data, then some other general results before we look into the different EWSs discussed in Chapter 2. Finally, we investigate the hysteresis that arises after loss of sea ice.

All results in this chapter are produced under the parameter regime that produces bifurcations, unless otherwise mentioned. This is achieved by removing the seasonal cycle in the models (Wagner and Eisenman, 2015b). With a seasonal cycle in the models there will not be a TP and therefore it does not make sense to look for EWSs in that scenario[1].

We will present results for four models, N81 with and without deep ocean, and WE15 with and without deep ocean.

1. It is possible to look for EWSs in parameter regimes that do not produce a TP. However, these EWSs will be false warnings (see Wagner and Eisenman (2015a)).

Model	A	B	D
N81	183.0	2.8	0.6
N81 w/deep ocean	188.5	2.4	0.66
WE15	182.0	2.9	0.6
WE15 w/deep ocean	192.5	2.5	0.66

Table 4.1: Adaption parameters

4.1 Fitting the Models

To get a proper representation in later experiments, we need to find the parameters that best reproduce our present and past climate. We apply historic forcing from the year 1880 to present (Hansen, 2007, 2011), and assume equilibrium between the mixed layer and deep ocean in 1880. We want to find the parameters that minimise the error to observed data, but it is also important to represent the present global temperature. Since all EBMs, and even ESMs, have a bias toward being too sensitive to volcanic activity (Marotzke and Forster, 2015) we can ignore the large temperature drop in the last decades of the 19^{th} century when we try to find the best fit. This is due to a number of large volcanic eruptions that occurred within two decades concluded by the Santa María eruption in 1902.

The fitted models to global temperature are shown in Figure 4.1a. All figures with multiple models in them will have the same colours for the models as in Figure 4.1a.

We can also look at more regional results, such as the polar regions ($64° - 90°$) shown in Figure 4.1b. Since the figure shows the mean of the Arctic and Antarctic regions the models are quite good at representing the rise in temperature. However, the variability of the observed temperatures are not captured by the models.

The parameters that fit best with observed global temperature (Morice et al., 2012) for each of the four models are shown in Table 4.1. As mentioned in

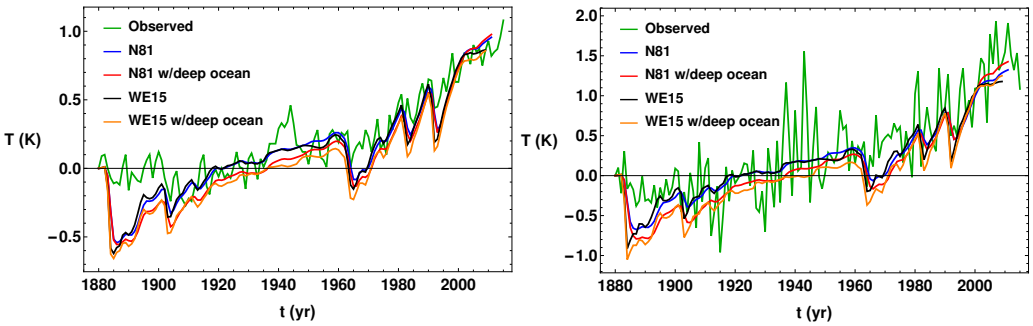

(a) Global temperature anomaly **(b)** Polar temperature anomaly

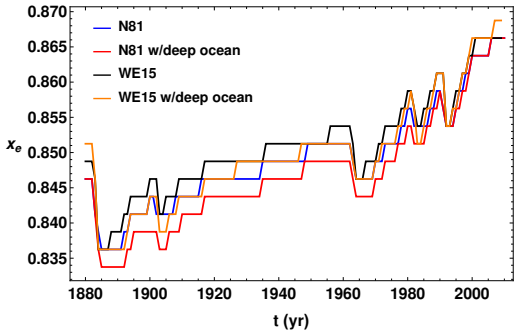

(c) Ice edge

Figure 4.1: Responses to historic forcing.

Chapter 3, we were able to increase the climate sensitivity (lower B) by adding a deep ocean coupling to N81 and WE15.

In Table 4.1 we can also see that we have a different diffusivity for each model. This is to achieve a similar ice edge between the models (within two grid points), see in Figure 4.1c. In the models with deep ocean some of the heat is taken out of the mixed layer near the equator, and there will be less heat transport northward. Hence with the same diffusivity, the ice edge will be further south in the models with deep ocean compared to the ones without. This is solved by having a slightly higher diffusivity in the models with deep ocean.

4.2 Response to Step Forcing

We will in this section look at the response of the models to a doubling and quadrupling pre-industrial CO_2 concentration, which corresponds to $3.7\,\mathrm{W\,m^{-2}}$ and $7.4\,\mathrm{W\,m^{-2}}$ given by the first order approximation of CO_2 forcing ($\Delta F = 5.35 \ln(C/C_0)$) (Huang and Bani Shahabadi, 2014). Since our models are inherently nonlinear the response is not necessarily proportional to the strength of the forcing.

In Figure 4.2a and Figure 4.2c there is no difference in the normalized response between the two scenarios. This means that we do not pass the TP in the models without deep ocean coupling. We also observe that the normalised temperature stabilises around $0.6\,\mathrm{K\,m^2\,W^{-1}}$. Thus the climate sensitivity is ~ 0.6.

In contrast, the models with deep ocean, shown in Figure 4.2b and Figure 4.2d have different climate sensitivity between the two scenarios. This can be attributed to the deep ocean heating, which heats the mixed layer past the TP in the quadrupling scenario. The additional heat gives a jump to ice-free conditions, seen in Figure 4.3b and 4.3d. In the quadrupling scenario stabilises

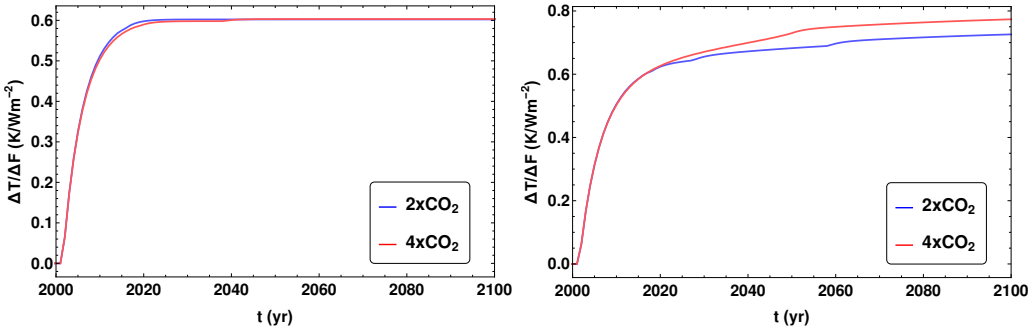

(a) N81 **(b)** N81 w/deep ocean

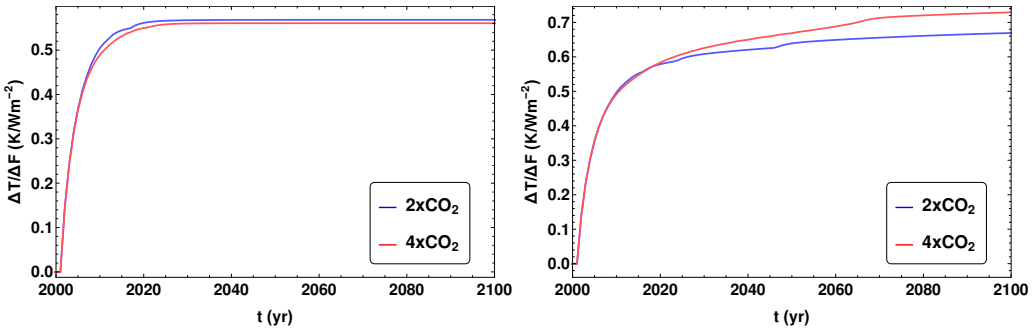

(c) WE15 **(d)** WE15 w/deep ocean

Figure 4.2: Normalised global temperature responses to doubling and quadrupling of CO_2.

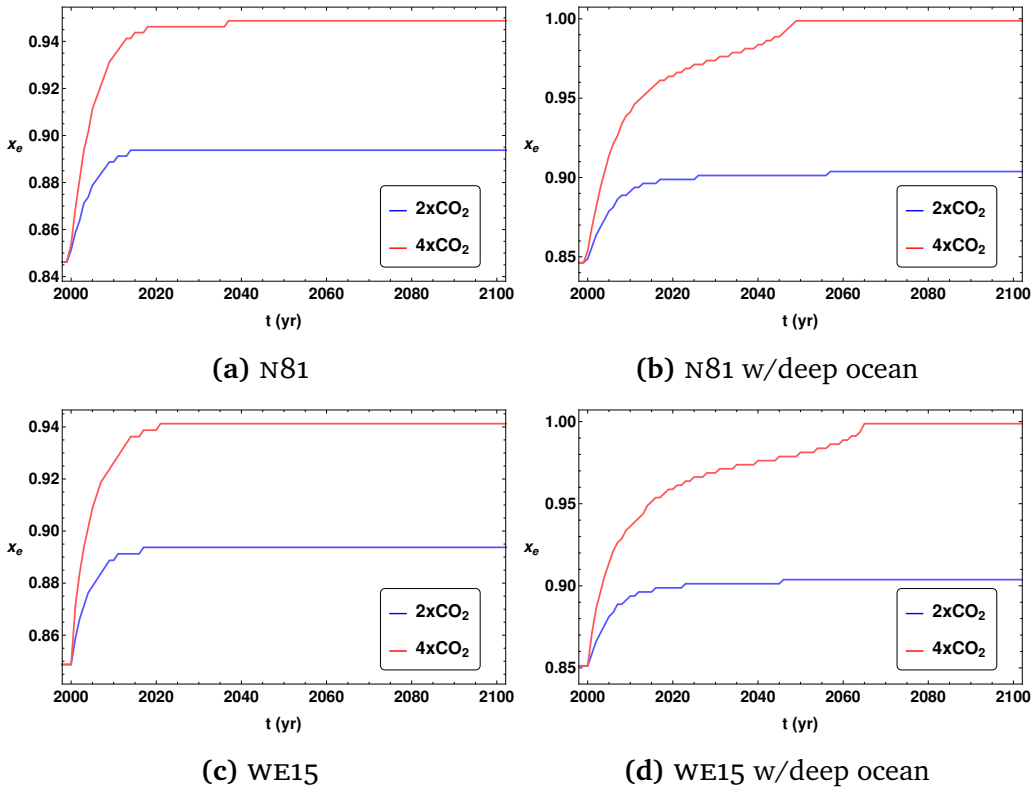

(a) N81 **(b)** N81 w/deep ocean

(c) WE15 **(d)** WE15 w/deep ocean

Figure 4.3: Ice edge responses to doubling and quadrupling of CO_2.

at $0.8\,\mathrm{K\,W^{-1}\,m^2}$ and $0.75\,\mathrm{K\,W^{-1}\,m^2}$ for N81 and WE15 respectively (out of frame in figures). Doubling of CO_2 leads to a climate sensitivity that is 0.05 lower than for the quadrupling scenario.

4.3 Early-Warning Signals

In this section, we will first consider the usual method for detecting EWSs using the Monte Carlo method. Then we will look into how our new EWSs behave when applied to observed and modelled data.

4.3.1 Monte Carlo Experiments

The conventional methods of detecting EWSs are to consider the increase in the variance and autocorrelation. Methods for computation of variance and autocorrelation are shown in Appendix B. We will now look at these methods for all four models.

We apply a linear forcing with added random noise in the form

$$n(t) = \sum_{k=0}^{T} w_k \cos(\pi k t/T), \;\; w_k \sim \mathcal{N}(0,1), \tag{4.1}$$

where T is the length of the simulation in years. This definition of noise will create oscillations on all time scales involved in the run, where each oscillation will have a random weight.

We chose to observe the pole temperature since this gives us the largest chance to catch an EWS. As mentioned it has been pointed out by Wagner and Eisenman (2015a) that ice area is not the best observable for detecting an EWS for the SICI.

N81

In this section, we will present the results from applying the forcing

$$f(t) = -0.5 + 0.03t + 0.2n(t) \tag{4.2}$$

to N81 with and without deep ocean coupling. We create 200 realizations for the ensemble.

In Figure 4.4, an increase in both variance and autocorrelation occurs way before the bifurcation point. At first glance, the plots with and without deep ocean look indistinguishable. We notice that N81 with deep ocean reaches the TP before the model without deep ocean. This is an example of the "heating in the pipeline" effect from the deep ocean thermal inertia, which will be

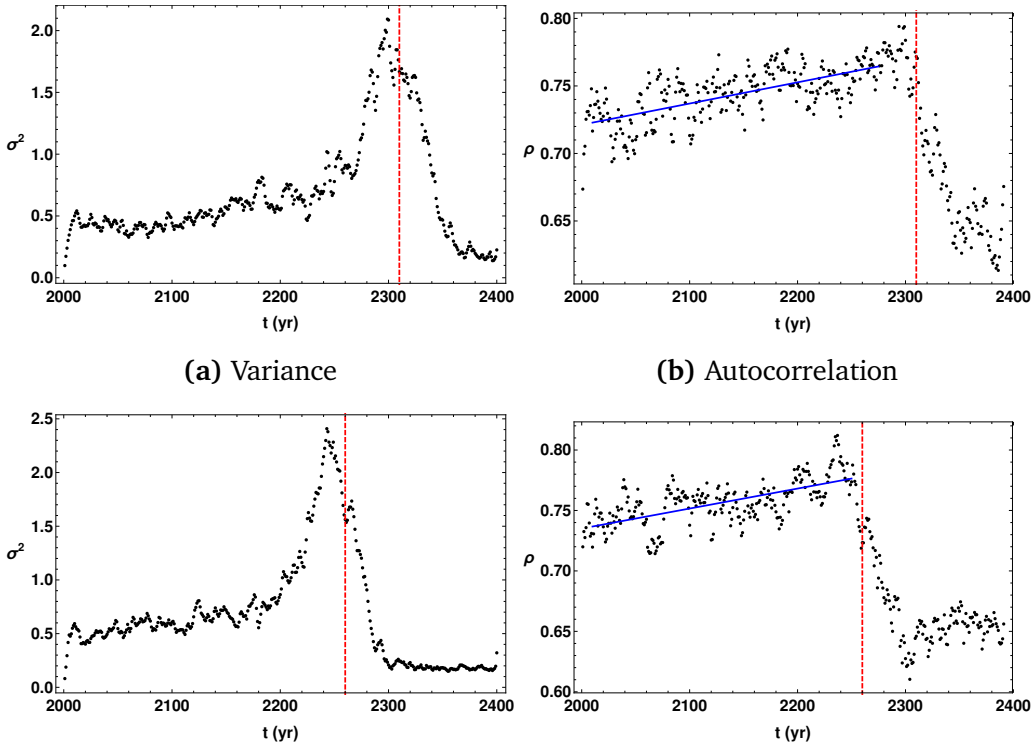

(a) Variance **(b)** Autocorrelation

(c) Variance w/ deep ocean **(d)** Autocorrelation w/deep ocean

Figure 4.4: Variance and autocorrelation of ensemble (200 realizations) pole temperature in N81.

Red dashed vertical line shows the bifurcation point of the ensemble mean. The blue lines show the best linear fit before this point.

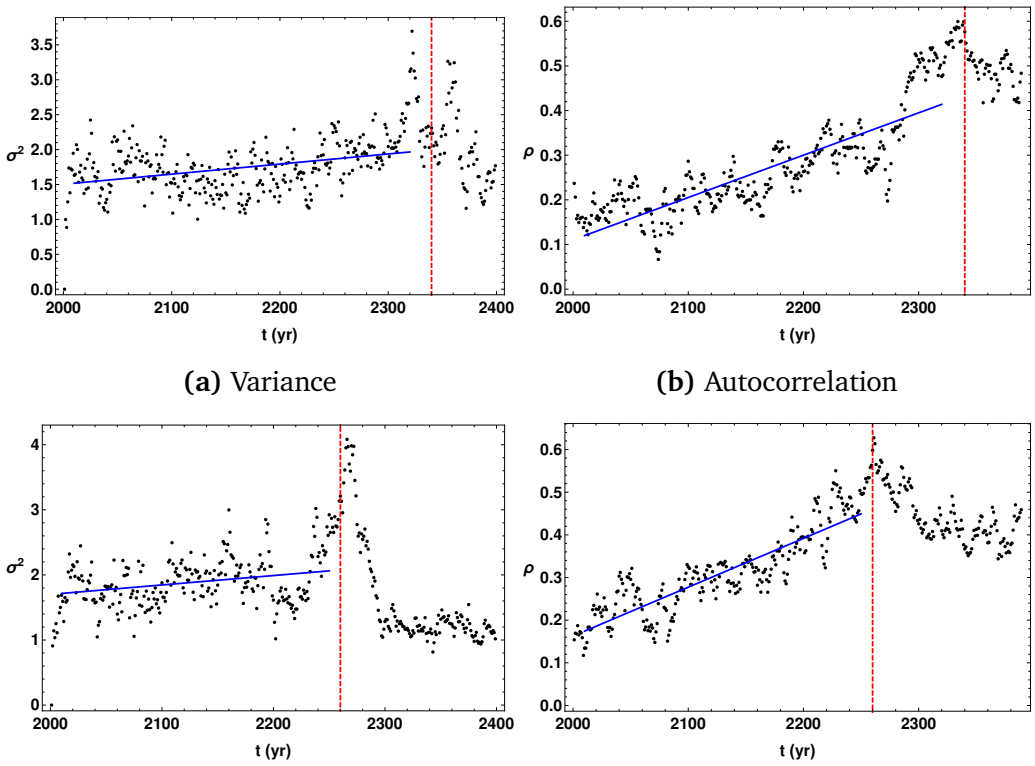

(a) Variance **(b)** Autocorrelation

(c) Variance w/deep ocean **(d)** Autocorrelation w/deep ocean

Figure 4.5: Variance and autocorrelation of ensemble (200 realizations) pole temperature in WE15.

Red dashed vertical line shows the bifurcation point of the ensemble mean. The blue lines show the best linear fit before this point.

discussed later. One other observation we can make is that the model with deep ocean has a slower transition from the linear rise to exponentiation rise in variance.

WE15

We do the same as in the section above with the two versions of WE15.

In contrast to Figure 4.4, there is only a small trend in Figures 4.5a and 4.5c. Using the methods shown in Appendix B the trend is not significant beyond

90% confidence.

Autocorrelation, on the other hand, has a stronger trend for WE15 than for N81. For autocorrelation, the trends are very prominent, in all models.

4.3.2 Polar Amplification

We will now look at the possibilities to predict a TP using polar amplification described in Section 2.3.1. We ramp the forcing by $0.03\,\mathrm{W\,m^{-2}\,yr^{-1}}$ to find the critical value of χ_T.

While trying to find tolerance level for χ_T we discover a problem with this EWS. There will be a lot of numerical noise when differentiating T_P and T_G. Hence, Figure 4.6 shows χ_T with a low-pass filter applied (cut-off frequency $\omega = 1/20\,\mathrm{yr}$).

4.3.3 Thin Ice Cap

In this section, we will look at the change in the ice cap described in Section 2.3.2. This effectively tells us something about the thickness of the ice cap ($A/V = 1/h$).

Historic

First, we observe how the EWS applied to historic sea ice data from the Arctic Ocean behaves. The sea ice area data is gathered from Fetterer et al. (2016), and the PIOMAS project has supplied the volume data (Schweiger et al., 2011).

Figure 4.7a shows the annual mean ice cap area and volume from 1979 to 2012 with linear trends. The data is normalised such that the axes represent the remaining fraction of the 1979 ice levels. We observe that the ice volume

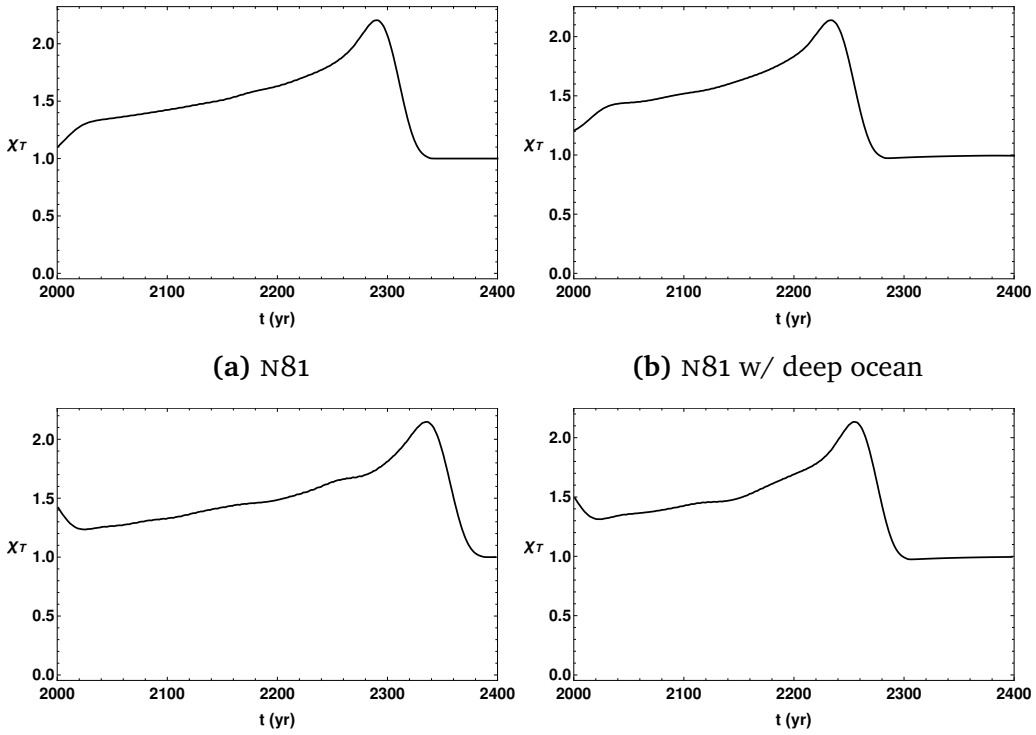

(a) N81 **(b)** N81 w/ deep ocean

(c) WE15 **(d)** WE15 w/ deep ocean

Figure 4.6: Regional temperature EWS, χ_T.

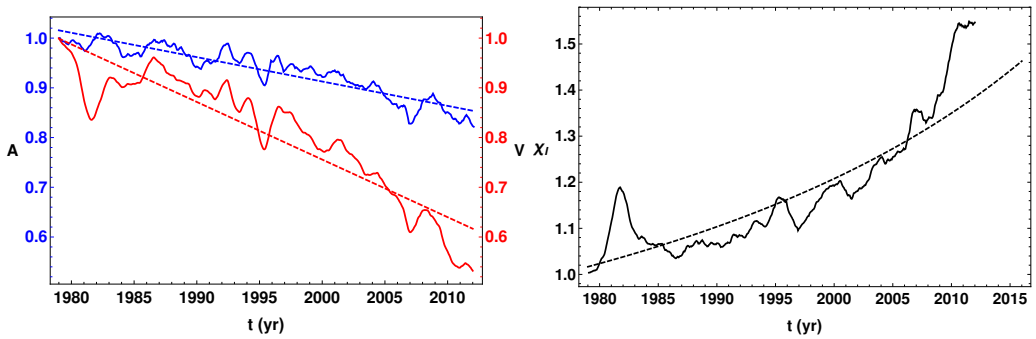

(a) Ice area and volume **(b)** χ_I

Figure 4.7: Normalised annual mean sea ice area and volume from observations.

(a) shows annual mean area in blue and volume in red. Dashed lines show the best linear fit for each. **(b)** shows the EWS magnitude, χ_I, solid line uses the entire data set, and the dashed line only uses the linear trends from **(a)**.

has decreased to about 60% of the 1979 level, while the ice area has only decreased to about 85% of the 1979 level. This indicates a thinning of the ice cap. The thinning is demonstrated by the EWS magnitude χ_I shown in Figure 4.7b.

Figure 4.8 shows the same as Figure 4.7 just for the annual minimum sea ice area and volume. Here we observe that the ice area is down to 75% of the 1979 level, while the volume is down a massive 65% to only about 35% remaining. This faster decrease implies that χ_I has risen faster than for annual mean, and with larger variance.

Simulated

We apply historic forcing (Hansen, 2007, 2011) to WE15[2], and observe how the EWS behaves when modelled.

2. Requires ice thickness. Thus, N81 is not included. In this short historic record there is little difference between the models with and without deep ocean. Thus the model with deep ocean is omitted.

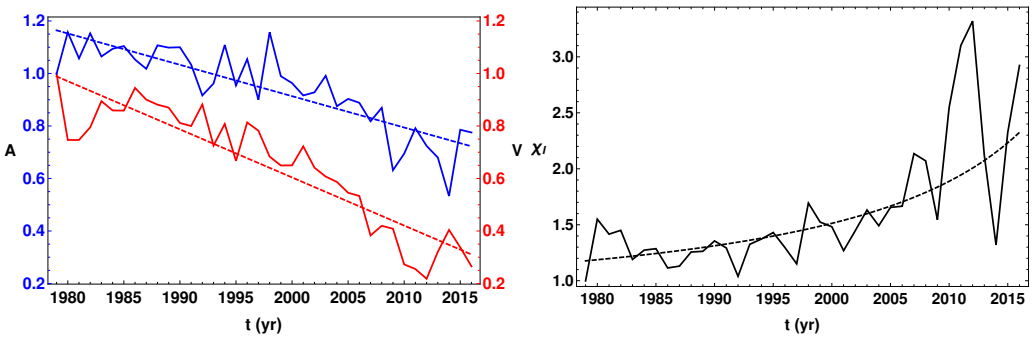

(a) Ice area and volume **(b)** χ_I

Figure 4.8: Normalised annual minimum sea ice area and volume from observations.

(a) shows annual minimum area in blue and volume in red. Dashed lines show the best linear fit for each. **(b)** shows the EWS magnitude, χ_I, solid line uses the entire data set, and the dashed line only uses the linear trends from **(a)**.

This time we will enable seasonality in the model such that we are able to observe the annual minimum sea ice extent.

We must also retune the model to fit the Northern hemisphere since this is where observations are from. This is done by increasing the climate sensitivity ($B \to 2.1$ (Wagner and Eisenman, 2015b)) since the Northern Hemisphere is warming faster that the Earth as a whole.

The trend lines for modelled area in Figures 4.9a and 4.10a agree reasonably with the observed data. Volume, on the other hand, does not match the observations, that well. This lack of ice mass loss leads to less rise of χ_I in Figures 4.9b and 4.10b.

We observe both in Figure 4.9a and 4.10a that there is greater correlation between the area and volume. In fact, the correlation is as high as 0.96 for the annual minimum. In contrast, the correlation between observed data is 0.81. It is natural that a model has higher correlation since there is no internal variability.

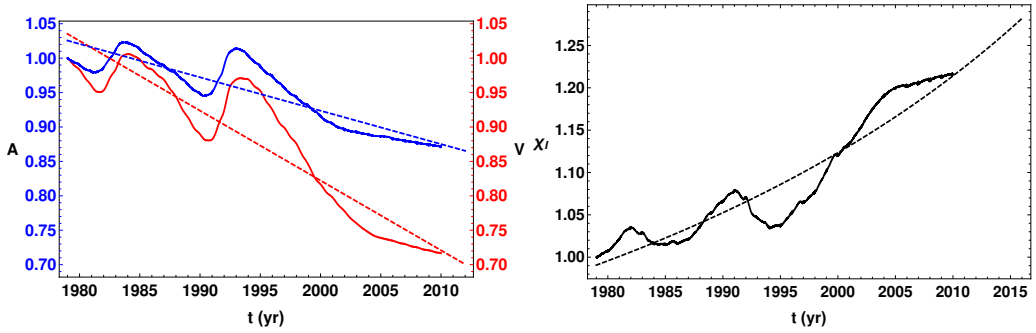

(a) Ice area and volume **(b)** χ_I

Figure 4.9: Simulated normalised annual mean sea ice area and volume from WE15.

(a) shows annual mean area in blue and volume in red. Dashed lines show the best linear fit for each. **(b)** shows the EWS magnitude χ_I, where solid line uses the entire dataset, and the dashed line only use the linear trends from **(a)**.

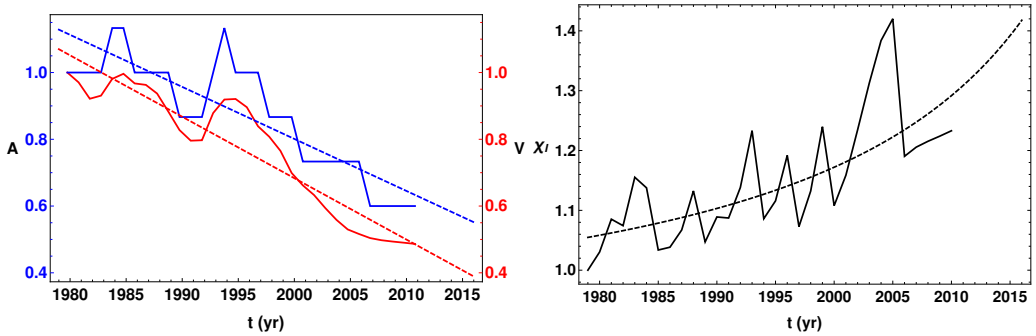

(a) Ice area and volume **(b)** χ_I

Figure 4.10: Simulated normalised annual minimum sea ice area and volume from WE15.

(a) shows annual minimum area in blue and volume in red. Dashed lines show the best linear fit for each. **(b)** shows the EWS magnitude χ_I, where solid line uses the entire dataset, and the dashed line only use the linear trends from **(a)**.

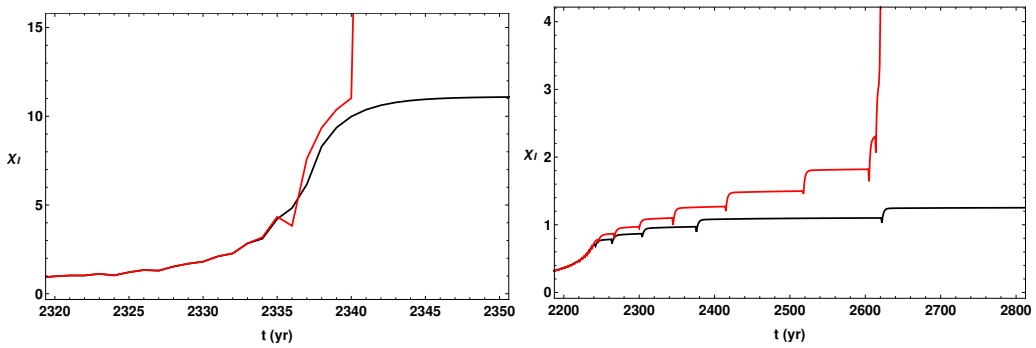

(a) WE15 without deep ocean **(b)** WE15 with deep ocean

Figure 4.11: χ_I for two different tolerance scenarios.

The red lines show the scenario where the bifurcation occurs, while black lines are where we barely save the ice cap. In **(a)** we stop forcing at $\chi_I = 2.1\,\mathrm{m}^{-1}$ (red) and $\chi_I = 2.0\,\mathrm{m}^{-1}$ (black). With deep ocean in **(b)**, we need top stop the forcing much earlier, at $\chi_I = 0.55\,\mathrm{m}^{-1}$ (red) and $\chi_I = 0.54\,\mathrm{m}^{-1}$ (black).

Point of No Return

When is it too late to stop forcing while perennially retaining the ice caps?

Let us monitor χ_I while ramping the forcing by $0.03\,\mathrm{W\,m^{-2}\,yr^{-1}}$, and terminating the forcing at different levels of χ_I to identify the latest point of retention of the ice caps.

We observe in Figure 4.11 that the tolerance for the model with deep ocean is much lower than without it. This is a consequence of the increased climate sensitivity introduced by the deep ocean, such as observed in Figure 4.2d.

We consider the ice area in Figure 4.12 and notice that the instability seems more significant in the model with deep ocean, i.e., the threshold for the bifurcation is further south, this leads us perfectly into the last section, which is where we look into the size of the hysteresis in WE15.

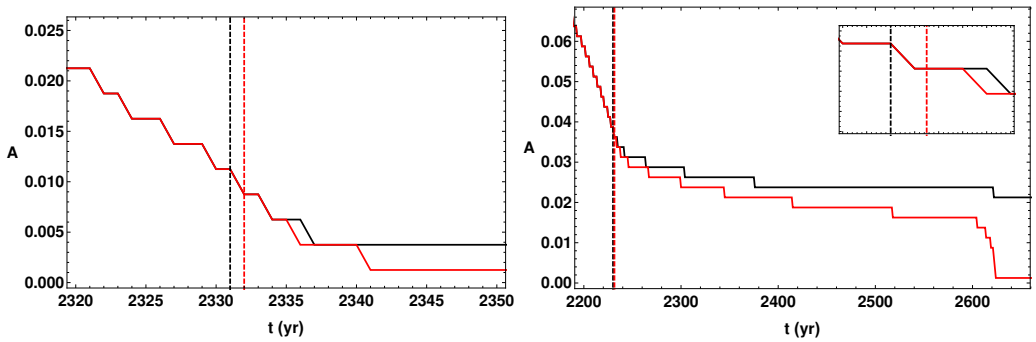

(a) WE15 without deep ocean **(b)** WE15 with deep ocean

Figure 4.12: Ice cap area for the tolerance test.

Colour indicate the same as in Figure 4.11. The dashed lines indicate when we stop forcing in the two scenarios. In **(b)** the dashed lines are so close that we have included a zoomed insert.

4.4 Time-Dependent Irreversibility

The irreversibility or the hysteresis width is defined as the forcing difference between the warming and the cooling pathway in the ice edge measured at a certain latitude. Thus the hysteresis width is

$$\Delta F = F_w - F_c. \tag{4.3}$$

F_w is the forcing in the first instance when the ice edge is north of $x_e = 0.985$. Consequently F_c is the forcing at the last instant the ice edge is north of $x_e = 0.985$. Having this set spot for measuring is a lot more intuitive than observing the sign of the pole enthalpy as Wagner and Eisenman (2015b).

We will present one scenario in the parameter regime where there is little to no irreversibility in the WE15[3], while adding the deep ocean coupling leads to a significantly larger irreversibility.

The scenario that is chosen has the default diffusivity ($D = 0.6\,\mathrm{W\,m^{-2}\,K^{-1}}$) with a slight seasonality in the forcing of $50\,\mathrm{W\,m^{-2}}$. The small seasonally kills all irreversibility in WE15 (Figure 6 in Wagner and Eisenman (2015b)).

3. If there is irreversibility in WE15 for certain parameters we can be positive that N81 has as well.

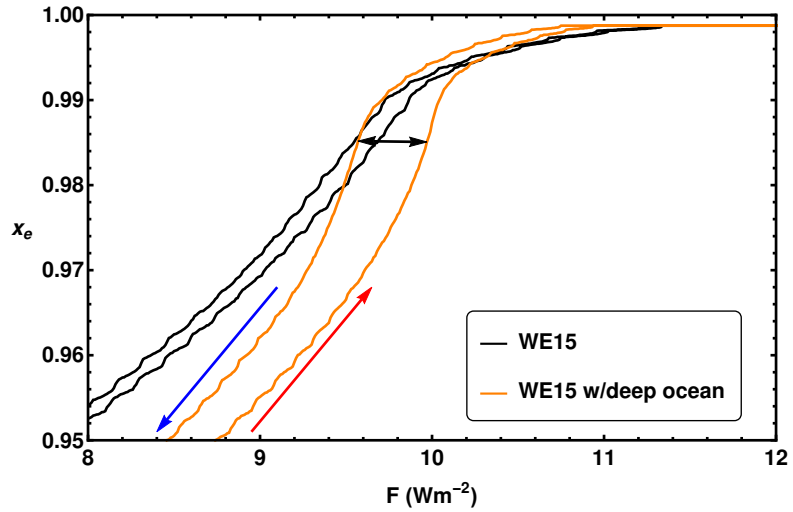

Figure 4.13: Irreversibility for slow ramp rate.

Arrows indicates ramp-up (red), ramp-down (blue), and the hysteresis width (black).

Slow Ramp Rate

Let us ramp up the forcing till perennially ice-free conditions and then down again. This is done at the slow rate of $0.01\,\mathrm{W\,m^{-2}\,yr^{-1}}$. This is done to ensure that the models always stay as close as possible to an equilibrium state.

Figure 4.13 shows the hysteresis path for the models. The hysteresis for the model with deep ocean is $0.42\,\mathrm{W\,m^{-2}}$ which is quite a bit larger than WE15 without deep ocean, which only has a hysteresis width of $0.13\,\mathrm{W\,m^{-2}}$. This is below the threshold of $0.2\,\mathrm{W\,m^{-2}}$ for hysteresis defined in Wagner and Eisenman (2015b).

Realistic Ramp Rate

In the perspective of anthropogenic global warming the slow ramp rate from above has no merit.

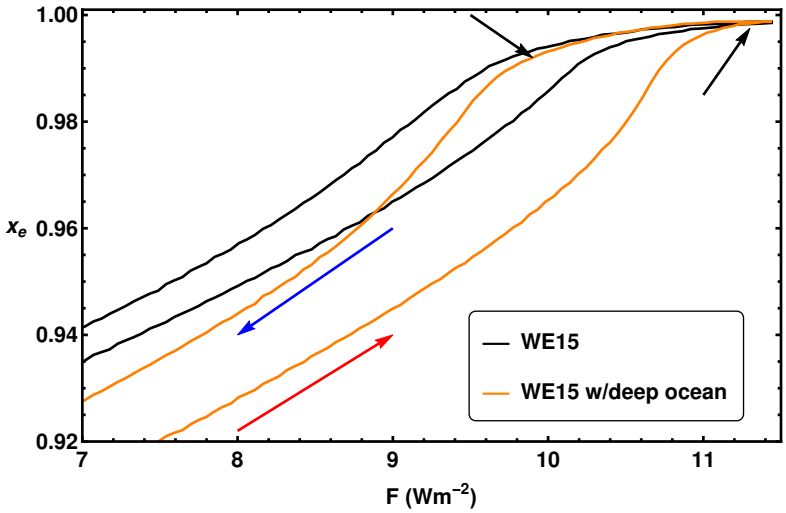

Figure 4.14: Irreversibility for fast ramp rate.

Arrows indicates ramp-up (red), ramp-down (blue), and the qualitative times we measure the hysteresis width (black).

We use the same model parameters as above[4], and increase the CO_2 concentration by 1% per year from 1880 to 2100. Subsequently the concentration is reduced to the pre-industrial at the same rate. This corresponds to a ramp rate of $0.052\,\mathrm{W\,m^{-2}\,yr^{-1}}$. The hysteresis width in Figure 4.14, measured between the two arrows, is $1.1\,\mathrm{W\,m^{-2}}$. This means that the ice returns about two decades later than it would if it had followed a reversible path.

This suggests that the hysteresis in WE15 with weak seasonality is a time-dependent effect (it depends on the ramp rate), and hence not a proper bistability.

4. Under standard seasonality ($338\,\mathrm{W\,m^{-2}}$), the response of the annual mean ice edge is linear.

5

Discussion and Analysis

This chapter will elaborate on the result described in Chapter 4.

5.1 Modelling

We will discuss the models in terms of fitting, derivation, and properties. Starting with the former.

5.1.1 Fitting the Models

For describing TP behaviour there is no difference between fitting the models to hemispheric or global temperatures. The reason we chose to adapt the models to the global temperature records is that global temperature records have a greater temporal span, and the forcing applied is a global average. This will hopefully lead to a better representation under other forcing scenarios.

N81

N81 is very predictable in the sense that if we increase the diffusivity the ice edge moves northward or vice versa. The same goes for the climate sensitivity. Changing B leads to a linear shift in the temperature response.

When adding a deep ocean to the model the fitting process is more difficult. Due to the longer time scale of the deep ocean, we must prolong the spin up time to reach equilibrium, from 200 yr to 2000 yr. This increase obviously leads to a longer execution time of the model. The amount of time required to fit the model becomes problematic.

WE15

All the challenges mentioned above is also true for WE15, and new issues arise with the addition of sea ice enthalpy. (3.17) illustrates this point, the temperature that separates the freezing and melting regimes depends on the OLR parameters.

So while juggling the ice edge and thickness, temperature, and the longer execution time of WE15 (for no noise spin up, see Figure A.1), it became clear that WE15 is a lot harder to adapt to the observed data.

We notice that the ice edge is quite low ($x_e = 0.87 \approx 61°$), but we must remember that we adapt the model to global temperature records and not the Northern Hemisphere (from 1880 to 2016 the mean temperature of the Northern Hemisphere has risen $\sim 0.5\,°C$ more than global average). For an experiment we must retune WE15 to the Northern Hemisphere, then the ice edge is much higher at $x_e = 0.95 \approx 72°N$.

Fitted Parameter Differences

Table 4.1 shows that there are slight differences between parameters used to fit N81 and WE15. This difference comes down to the key difference between the models, the ice thickness.

Changing the OLR is the tool we have to fit the models to observed temperature. Adapting the temperature dependent part, B gives us the ability to ensure correct climate sensitivity in the models. In N81 all the energy added goes into the mixed layer or the deep ocean. WE15 has the extra component of ice enthalpy. Thus there is more components to heat. Since B is smaller in WE15 than in N81 we conclude that it takes more energy to heat ice and mixed layer than just the mixed layer.

The non-temperature dependent part of the OLR, A is adjusted to achieve the proper non-normalized temperature, which was 13.74 °C in 1880. All the models are within 0.2 °C of this.

Adding a deep ocean to both models leads to an unexpected change in the location of the ice edge. This can be attributed to the coupling factor, κ which is defined as a logistically decreasing function toward the pole, such that there is no heat exchange outside a 30° band around the equator. Hence the coupling only takes energy out of this band and diverts it into the deep ocean, resulting in a weaker northward transport. As a result of this weakening, the ice edge moves slightly southward. We solve this by increasing the diffusivity somewhat.

We can see in Figure 4.1a that the sensitivities of the models are slightly different, so going to one more decimal place in the OLR parameters would have been beneficial.

In the high latitudes (Figure 4.1b), the models represent the rise in temperatures properly (mean of Arctic and Antarctic). However, the variability in the models is nowhere close to the one observed. This lack of variability means that

there are other mechanisms than the ice-albedo feedback that affect the high latitude temperatures. Also, under the retuning to the Northern Hemisphere the models are not even able to capture the rise in temperature.

5.1.2 Global vs. Northern Hemisphere

Due to the sensitivity difference when fitting the models to either the global or the Northern Hemisphere temperatures, the behaviour differs slightly with respect to which latitude the ice cap is unstable. North (1984) and Wagner and Eisenman (2015b) show that the ice cap is unstable at $75^\circ N$ and $78^\circ N$, respectively. In Figure 4.12a, which shows global ice area, we observe that the ice cap is stable up to 84° in WE15 without deep ocean. However, when considering the model with deep ocean (Figure 4.12b), we can see that the instability occurs at lower latitudes $\sim 80^\circ$. This observation suggest that the stability of the ice caps is related to the climate sensitivity in the mixed layer. A higher sensitivity (lower B) will increase the effect of the ice-albedo feedback and therefore induce increased instability in the ice cap. This means that adding a deep ocean coupling to the models will affect the stability of the ice cap.

5.1.3 Sea Ice and Deep Ocean

In the first attempt at adding a deep ocean to WE15, we replaced the constant ocean heating, F_b in (3.12), by the dynamic coupling, $\kappa(T - T_d)$. This leads to unexpected behaviour in the model. The sea ice thickness goes unstable and grows unbounded. After some investigation, it became clear that F_b does not affect the calculation of the surface temperature of the ice, T_0, as derived in Section 3.2.2. However, what is affected by F_b is the enthalpy. Since (3.12) is valid everywhere, by removing the constant deep ocean heat, the enthalpy becomes more negative under the ice, which leads to an increase in ice thickness by relation (3.11).

To solve this issue we have to keep both the constant deep ocean heating and the dynamic coupling.

5.1.4 Climate Sensitivity in Models

The deep ocean coupling term in (3.1)/(3.12) is negative and therefore takes energy out of the mixed layer. Thus we must reduce the OLR parameters to achieve the same fit to observed data, and the energy imbalance at the top of the atmosphere increases.

The delayed heating begins when the deep ocean cannot remove more heat from the mixed layer. Then the increased energy imbalance will provide additional heating of the mixed layer. This is what is called "the heating in the pipeline."

We notice in Figures 4.4 and 4.5 that the models with deep ocean reach the TP a good 50 yr earlier than the models without deep ocean. This extra heating is not noticeable in the historic runs of the model, and it should not be because the point of adding a deep ocean to N81 and WE15 is that we have this additional heating.

We can see in Figure 4.2 that the models with deep ocean more closely represent the climate sensitivity that we see in the ensemble of ESMs, which is ~ 0.8 (Rahmstorf, 2008). The upper bound in Figure 2.2 is large, which leaves a lot of room for the possibility of larger deep ocean heat capacity.

5.2 Early-Warning Signals

5.2.1 Conventional

In the warming scenario that we apply to the models, the ice shrinks and finally disappears suddenly at the TP. To look at the ice area as an EWS

as Wagner and Eisenman (2015a) did during this warming is not beneficial since less ice leads to less possibility for variance (the same is true for ice volume).

We rather observed that the variance and autocorrelation in the pole temperature, gives us the best possibilities to detect an EWS. Polar temperatures still have a strong rise in variance and autocorrelation for N81. We even observe the TP when looking at global temperatures, but there is no trend in the variance and autocorrelation.

Since the rise is variance in WE15 is already marginally significant, going to polar temperatures the trend cannot be detected.

Thermodynamics tells us that to increase the temperature of an icy water column, we first need to melt all the ice in the column. This is the reason why seasonal ice minima occur in September and maxima occur in Mars. In WE15 this effect will create a delay, after some force is applied, in the temperatures in the ice region. It is possible to see this effect in Figure 4.2. It takes slightly longer to reach equilibrium in WE15 than in N81. This mechanism explains why there is less rise in variance in WE15 than in N81. This process is confirmed for summer ice in a simpler model than WE15 by Bathiany et al. (2016).

5.2.2 Thin Ice Cap

There are clearly other mechanisms that affect the observed ice area and volume, since applying historic forcing to WE15 did not replicate the magnitude of the volume loss. This is a general problem of using an aqua planet model. The Arctic Ocean is not an open ocean. We can attribute the increased loss of ice mass, in observed data, to the seasonal outflow trough the Fram Strait, which is responsible for up to 90% of sea ice export from the Arctic Ocean (Gyory et al., 2013).

The point of no return for WE15 without deep ocean is $\chi_I \approx 2.0\,\mathrm{m}^{-1}$. While the observed annual mean is getting close to $\chi_I \approx 1.5\,\mathrm{m}^{-1}$, and the annual minimum is $\chi_I \approx 2.3\,\mathrm{m}^{-1}$. So if we disregard the deep ocean in the model, it may be possible to save some seasonal sea ice cover.

WE15 with deep ocean has a point of no return at $\chi_I \approx 0.55\,\mathrm{m}^{-1}$. Even though it may take a while before we lose the ice cap, this analysis shows that it will certainly happen.

5.3 Time-Dependent Irreversibility

It is natural that a large thermal inertia will resist the ramp-up and ramp-down in forcing, so a larger hysteresis with larger thermal inertia is no surprise.

One of the factors that will affect the hysteresis width is how fast we ramp-up or down. In Figure 4.13 we ramp-up with the slow rate of $0.01\,\mathrm{W\,m^{-2}\,yr^{-1}}$ while in Figure 4.14 the rate is $0.052\,\mathrm{W\,m^{-2}\,yr^{-1}}$. This greatly affect the hysteresis width. Figure 4.14 is more politically relevant since it concerns human time scales and not the thousands of years in Figure 4.13. The fact that Figure 4.14 has a larger hysteresis width gives us an indication of when we can expect the ice to return in a carbon capture and storage (negative emissions) scenario. The same scenario as shown in Figure 4.14 was conducted with double heat capacity in the deep ocean. However, this did not result in a significantly wider hysteresis.

We tested for irreversibility in two scenarios other than the one seen in Figure 4.13. These were one with high seasonality and low diffusion ($S = 338\,\mathrm{W\,m^{-2}}$, $D = 0.075\,\mathrm{W\,m^{-2}\,K^{-1}}$), and one with intermediate values ($S = 100\,\mathrm{W\,m^{-2}}$, $D = 0.2\,\mathrm{W\,m^{-2}\,K^{-1}}$). But as concluded by Wagner and Eisenman (2015b), even a slight diffusion ($D = 0.1\,\mathrm{W\,m^{-2}\,K^{-1}}$) will kill all hysteresis in scenarios with seasonality over $150\,\mathrm{W\,m^{-2}}$. The same seems true for the model with deep ocean. The diffusivity is more important for keeping the

hysteresis in the model with deep ocean. This is because heat exchange only occurs near the equator. Thus with low diffusivity, no heat from the deep ocean will affect the ice in the high latitudes. Changing the way the mixed layer and deep ocean are coupled can change the hysteresis at low diffusivity.

We would like to reproduce Figure 6 from Wagner and Eisenman (2015b) with the addition of deep ocean to WE15. The 441 simulations will take an approximately 200 days using the same computing power used under the entire thesis. More on this in the next section.

5.4 Spatial Model Resolution

We chose to use the same number of gridpoints, 400, as Wagner and Eisenman (2015b) for all the experiments. In retrospect, this decision may have been hasty.

As plenty of cartographers have realised it is impossible to project a sphere onto a plane, while keeping all the proportions correct. In the models, we project a curve onto a straight line. Evenly spacing the projections ($x \in [0, 1]$) and not the latitudes makes us able to use the Legendre diffusion operator for a sphere. Using 400 gridpoints gives us only five gridpoints from 80° to 90°, and the last jump is from 85° to the pole.

When we observe temperatures the resolution is not a huge problem, since we either observe the temperature at a point or an average over a large area. The smooth nature of diffusion keeps the temperature gaps between gridpoints to a minimum. Sea ice area, on the other hand, is something that moves with the same resolutions as the model. Moreover, having the ice edge move up to five degrees in one timestep is not beneficial.

Some of the TPs relating to the ice area seen in Chapter 4 are not very pronounced, but by converting back to latitudes they become unmistakable.

Increasing the resolution leads to a massive escalation of the computation time. Theoretically solving a tridiagonal matrix system, like ours, has the complexity of $O(n)$ (Thomas, 1949). As shown in Figure A.1 this is far from the truth for the algorithms described in Appendix A. There is clearly some overhead in the algorithms. Without further investigation we figure that this overhead occurs due to algorithmic checks for certain matrix properties. We can solve this in the future by implementing a custom solver.

6

Concluding Remarks

6.1 Summary

We have shown that there are some areas where the models studied here come to short, namely the description of high latitude temperatures. This indicates that the observed polar amplification is caused by other mechanisms than just the ice-albedo feedback which is yet to be understood in GCMs (Boé et al., 2009).

EWSs are possible to detect for the SICI either in form of rising variance and autocorrelation for pole temperatures, or the thinning of the ice cap in WE15. We can predict the bifurcation to ice-free conditions using the rate of change in regional temperatures. However, observing it continuously is not possible due to numerical properties of the models.

WE15 is not able to capture the outflow of ice mass through the Fram Strait, resulting in underestimation of the thinning of the ice cap.

The deep ocean heating cannot be omitted when investigating the irreversible evolution of the sea ice cover in ramp-up/ramp-down scenarios.

Model resolution is an issue in high latitudes, we should increase the resolution for future experiments. Using a faster framework to avoid an exponential rise in runtime should be considered.

6.2 Concluding remarks

Adding a deep ocean coupling to N81 and WE15 has no profound effect on the ability to detect EWSs for the SICI. What it does affect is the climate sensitivity and thereby the ability we have to stop the ice caps from disappearing. It also slows the regeneration of the sea ice cover in negative emission scenarios where the CO_2 concentration is returned to the present level.

A transition in sea ice cover is predicted by some of the models, and now we have a better understanding of the effort required to return to a perennial ice cap.

We now have a better understanding of what initiates the TP in WE15. Even though the model does not exhibit the same ice volume as observations under historic forcing. We can use the thinning of the ice cap in the model to indicate the imminence of a TP. Hence it may be appropriate to rename the SICI to the thin ice cap instability.

6.3 Further work

There are plenty of further expansions of the models that can be done.

The most interesting would be to expand the models to 2D, such that we can perturb the ice cap in space.

To properly represent the high latitudes we might have the OLR parameters dependent in space, or have more complex diffusion patterns.

Some years ago it seemed that GCMs could not predict the massive loss of sea ice that was occurring. However, the inclusion of melt ponds in GCMs results in a proper representation of recent decline in ice area (Flocco et al., 2010). In WE15 we could incorporate this as random open water or ice in the melting regime.

A

Implementation of Models

In this appendix, we will show the numerical methods used to solve the two models N81 and WE15. Both models consists of two coupled PDEs. The diffusion equation has a nonlinear temperature dependence, $\alpha(x, x_e(T))$. This dependence is the result of the temperature dependence of the ice-edge position $x_e(T)$, which is found by (numerically) solving the equation $T(x) = 0$. The systems are *not* trivial to solve, in fact, they can only be solved numerically in the default parameter regime. By either removing the seasonal cycle or the diffusivity the system can be solved using Legendre polynomials.

A.1 Implementation of N81

We will use the method of lines (MOL) to implement this simpler model. The MOL technique consists of discretizing all spatial dimensions and leaving the time dependence unchanged. We use this to turn (3.1) and (3.10) into a large

coupled system of ordinary differential equations (ODEs).

$$\begin{aligned} c_w \frac{\mathrm{d}T_i}{\mathrm{d}t} &= -A - BT_i + \alpha(x_i, x_{e,i})S(t, x_i) \\ &\quad + D\Big[- x_i \frac{T_{i+1} - T_{i-1}}{\Delta x} + (1 - x_i^2)\frac{T_{i+1} - 2T_i + T_{i-1}}{\Delta x^2}\Big] + \kappa(T_i - T_{d,i}) + F, \\ c_d \frac{\mathrm{d}T_{d,i}}{\mathrm{d}t} &= \kappa(T_i - T_{d,i}), \end{aligned} \tag{A.1}$$

where the spatial grid is defined as

$$x_i = i\Delta x,\ \Delta x = 1/N \tag{A.2}$$

where N is the size of the grid. We can rewrite (A.1) in matrix form

$$\begin{aligned} c_w \dot{\boldsymbol{T}} &= D\mathcal{M}\boldsymbol{T} + f(\boldsymbol{T}) + \kappa \boldsymbol{T}_d,\ f(\boldsymbol{T}) = -A - (B + \kappa)\boldsymbol{T} + \alpha S, \\ c_d \dot{\boldsymbol{T}}_d &= \kappa \mathcal{A}\boldsymbol{T}_d + \kappa \boldsymbol{T}. \end{aligned}$$

Combining the above equations into one system of coupled ODEs

$$\begin{pmatrix} c_w \dot{\boldsymbol{T}} \\ c_d \dot{\boldsymbol{T}}_d \end{pmatrix} = \begin{pmatrix} D\mathcal{M} & \\ & \kappa\mathcal{A} \end{pmatrix} \begin{pmatrix} \boldsymbol{T} \\ \boldsymbol{T}_d \end{pmatrix} + \kappa \begin{pmatrix} \boldsymbol{T}_d \\ \boldsymbol{T} \end{pmatrix} + \begin{pmatrix} f(\boldsymbol{T}) \\ 0 \end{pmatrix} \tag{A.3}$$

where $\mathcal{M}$ is a $N \times N$ tridiagonal difference matrix with non-zero components (Bitz and Row, 2001)

$$\begin{aligned} m_{j,j-1} &= \lambda_{j-1}, && j = [2, N], \\ m_{j,j} &= -(\lambda_{j-1} + \lambda_j), && j = [2, N-1], \\ m_{j,j+1} &= \lambda_j, && j = [1, N-1], \\ m_{1,1} &= -\lambda_1, \\ m_{N,N} &= -\lambda_{N-1}, \end{aligned} \tag{A.4}$$

where $\lambda_j \equiv (1 - x_j^2)/\Delta x^2$. From (A.1) we can see that $\mathcal{A}$ will simply be a $N \times N$ matrix with -1 on the diagonal, zero elsewhere. (A.3) can now be solved by using general-purpose ODE solver. The LSODA ode solver (Brown and Hindmarsh, 1989; Hindmarsh, 1983) adapts its method depending on whether the problem is stiff or non-stiff. This means that when (A.3) has

stabilized the solver can take much larger steps in time and thereby cutting down on runtime.

The initial value for the system is set as

$$T(0,x) = 7.5 + 20(1 - 2x^2),$$
$$T_d(0,x) = T(0,x).$$

Assuming equilibrium between mixed layer and deep ocean before additional forcing is applied.

A.2 Implementation of WE15

The implementation of WE15 is somewhat different to that of N81 due to the ice thickness (we will strictly show the differences, the remainder is the same as for N81). (3.12), (3.17) and (3.18) are the governing equations of WE15.

A.2.1 Ghost Layer

We introduce a ghost layer and let the spatial diffusion work in this layer (see Appendix A in Wagner and Eisenman (2015b)). This technique is strictly a numerical one, and not a substitute for an atmosphere. The ghost layer has a temperature, T_g which evolves as

$$c_g \frac{\partial T_g}{\partial t} = \frac{c_g}{\tau_g}(T - T_g) + D\nabla^2 T_g, \tag{A.5}$$

where c_g is the heat capacity of the ghost layer. c_g is much smaller than the heat capacity of the mixed layer, see Table 3.1. τ_g is the coupling coefficient between the two layers, which is kept very fast in this model since this technique is strictly numerical. We can now replace the diffusive term in (3.12) with the coupling term $-\frac{c_g}{\tau_g}(T - T_g)$.

A.2.2 Freezing Temperature

T_0 can be calculated from (3.17). Replacing the diffusion with the ghost layer, and $h = -E/L_f$ gives the solution

$$T_0 = \frac{\alpha S - A + F + \frac{c_g}{\tau_g} T_g}{B + \frac{c_g}{\tau_g} - \frac{kL_f}{E}}. \tag{A.6}$$

This is used to find whether the ice is freezing or melting from (3.18).

A.2.3 Time-Stepping Scheme

To advance the enthalpy in time we use the forward Euler method

$$E_{i+1} = E_i + \Delta E_i, \tag{A.7}$$

where

$$\Delta E_i = \Delta t (C_i - (B + \frac{c_g}{\tau_g} + \kappa) T_i + F), \tag{A.8}$$

$$C_i = \alpha S_i - A + \frac{c_g}{\tau_g} T_{g,i} + \kappa T_{d,i} + F_b. \tag{A.9}$$

Evaluating C_i at times $t_i = (i + 1/2)\Delta t$.

The time evolution of the ghost layer temperature T_g is computed using the implicit backwards Euler method

$$T_{g,i+1} = T_{g,i} + \Delta T_{g,i+1}. \tag{A.10}$$

Discretizing (A.5) and inserting into (A.10) yields

$$T_{g,i+1} = T_{g,i} + \Delta t \left[\frac{1}{\tau_g} (T_{i+1} - T_{g,i+1}) + \frac{1}{c_g} D \nabla^2 T_{g,i+1} \right]. \tag{A.11}$$

Inserting (3.18) into (A.11) and solving for $T_{g,i+1}$, we obtain

$$T_{g,i+1} = M_1^{-1} M_2, \tag{A.12}$$

where M_1 and M_2 are found to be

$$M_1 = \left[\phi_{\text{all}} - \frac{\Delta t c_g}{\tau_g^2}\text{diag}\left(\frac{1}{B + \frac{c_g}{\tau_g} - \frac{kL_f}{E_{i+1}}}\right)_{E<0,T_0<0}\right],$$
$$M_2 = \left[T_{g,i} + \frac{\Delta t}{\tau_g}\left(\frac{E_{i+1}}{c_w}\right)_{E>0} + \frac{\Delta t}{\tau_g}\left(\frac{\alpha S_{i+1} - A + F}{B + \frac{c_g}{\tau_g} - \frac{kL_f}{E_{i+1}}}\right)_{E<0,T_0<0}\right].$$

$$\phi_{\text{all}} = (1 + \frac{\Delta t}{\tau_g} + \Delta t\kappa)\mathcal{I} - \frac{\Delta t}{c_g}D\mathcal{M}$$

where $\mathcal{I}$ and $\mathcal{M}$ are the identity matrix and the difference matrix respectively. ϕ_{all} is the only quantity that does not depend on time, all other terms needs to be computed for every timestep.

We again use the Euler method to iterate (3.10), such that

$$T_{d,i+1} = T_{d,i} + \Delta t\frac{\kappa}{c_d}(T_i - T_{d,i}). \tag{A.13}$$

The initial value for this system is

$$\begin{aligned} T(0,x) &= 7.5 + 20(1 - 2x^2), \\ T_g(0,x) &= T(0,x), \\ T_d(0,x) &= T(0,x), \\ E(0,x) &= c_w T(0,x). \end{aligned}$$

We now iterate (A.9), (A.6), (A.13), (A.8), and (A.12), in that order. T is found using (3.18).

We run the models such that T and T_d are in an equilibrium before we start applying additional radiative forcing. If we define zero forcing before the industrial revolution, it can be considered approximately true that the mixed layer and deep ocean are in equilibrium at that time.

The source code for the models can be found on GitHub[1][2].

1. N81: `https://github.com/Erik-BM/north_model`
2. WE15: `https://github.com/Erik-BM/we_model`

A.3 Spatial and Temporal Resolution

Since the ice edge is defined by either the temperature or the enthalpy, depending on the model, we need to have a high spatial resolution to stop the ice edge from moving far between from one timestep to another. We also need to strike a balance between resolution and runtime of the models, with $N = 400$ spatial points this balance is optimal.

The spatial resolution is kept the same in both models, however, due to stability conditions of the Euler method the temporal resolution needs to be higher for WE15. While in N81 we get away with $\Delta t = 0.01$ yr or even less, in WE15 the resolution is required to be ten times higher to ensure convergence of the Euler method.

A.4 Runtime

We will look at the runtime it takes simulate 400 years of linear forcing with and without noise. As we can see in Figure A.1 that the runtime is very model and forcing dependent.

Due to the method used to solve WE15, it does not matter what forcing we apply to the model, and all of the times are close. N81 is another story, the solver used can make assumptions depending on the right-hand side of (A.3), but when the forcing is noisy, this is not possible, and the solver assumes a worst case scenario. This results in a runtime that is up to eight times longer than for the run without noise. The difference between N81 with and without deep ocean is due to that the deep ocean will double the size of (A.3), and therefore will take longer to solve for each timestep.

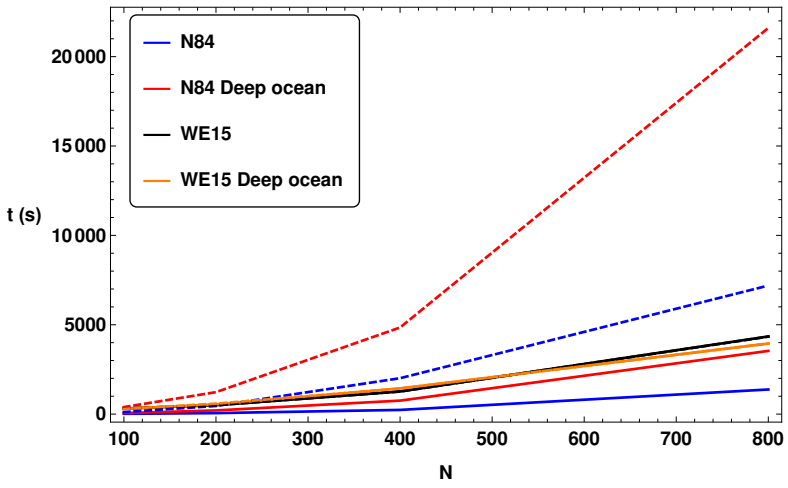

Figure A.1: Runtime

The horizontal axis shows the number of gridpoints (simulations for $N \in [100, 200, 400, 800]$). The vertical axis shows runtime in seconds. Colours indicate the permutations of the models. Solid lines indicate forcing without noise, while the dashed lines are to indicate noisy forcing.

B

Calculation of σ^2 and ρ

The variance, σ^2 is straightforward to calculate, we simply take the square of each ensemble member subtracted from the time series without noise. Then we take the mean of the variances to get the mean of the ensemble variance.

$$\sigma^2 = \frac{1}{N}\sum_{i=0}^{N-1}(X_i - \bar{X})^2, \tag{B.1}$$

where N is the ensemble size, X_i is each ensemble member, and $\bar{X}$ is the run without random noise.

Autocorrelation, ρ is not as straightforward to calculate. We calculate the autocorrelation as the correlation between two lag 1 offset windows in the

time series.

$$
\begin{aligned}
X_{j,i,1} &= [x_{j,i+1}, \ldots x_{j,i+p}], \\
X_{j,i,2} &= [x_{j,i}, \ldots, x_{j,i+p-1}], \\
R_j &= [\mathrm{corr}(X_{j,0,1}, X_{j,0,2}), \ldots, \mathrm{corr}(X_{j,M-p-1,1}, X_{j,M-p-1,2})], \\
\rho &= \frac{1}{N} \sum_{j=0}^{N-1} R_j,
\end{aligned}
\tag{B.2}
$$

where x_j is ensemble member j, p is the window length (10 yr in this thesis), and M is the length of x_j.

To verify that we have convergence in in the variance and autocorrelation we create 200 ensembles of size 100 drawn randomly from the full ensemble (200 realisations). Then we calculate the trend of the variance and autocorrelation in each of the 200 ensembles. The trends for all the permutations of the models are shown in Figure B.1.

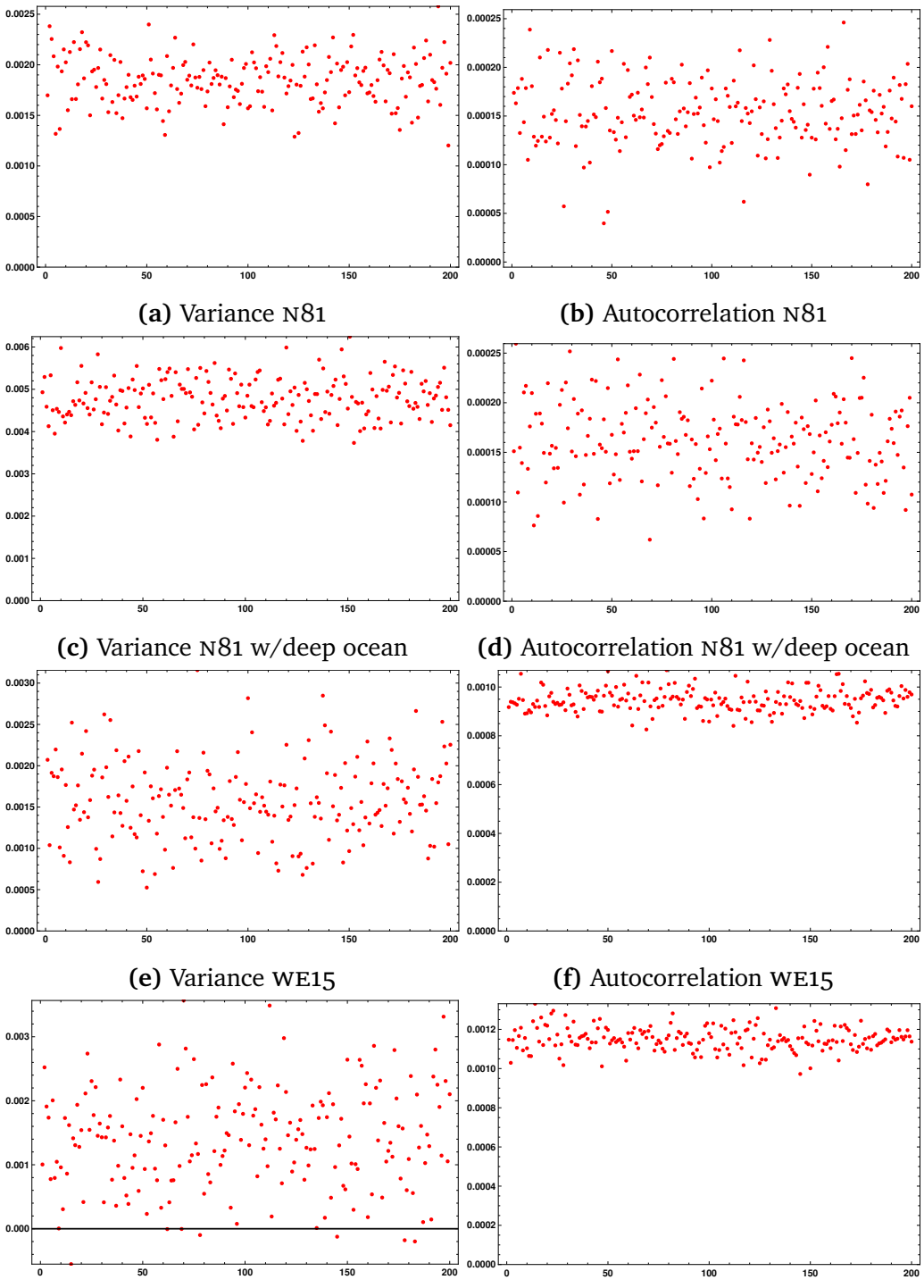

(a) Variance N81

(b) Autocorrelation N81

(c) Variance N81 w/deep ocean

(d) Autocorrelation N81 w/deep ocean

(e) Variance WE15

(f) Autocorrelation WE15

(g) Variance WE15 w/deep ocean

(h) Autocorrelation WE15 w/deep ocean

Figure B.1: Test of convergence for σ^2 and ρ in pole temperature.

The horizontal axis measures the trend in variance or autocorrelation for each of the randomly picked 200 ensembles of size 100. All figures except **(g)** show that all the ensembles have positive trends with greater than 99% confidence. **(g)** has five ensembles with a negative trend and five with neutral trend such that we can say we have positive trends within 90% confidence.

Bibliography

Bathiany, S., B. van der Bolt, M. S. Williamson, T. M. Lenton, M. Scheffer, E. H. van Nes, and D. Notz
2016. Statistical indicators of arctic sea-ice stability – prospects and limitations. *The Cryosphere*, 10(4):1631–1645.

Bitz, C. and G. Row
2001. Ice and climate modeling: Course notes.

Boé, J., A. Hall, and X. Qu
2009. Current gcms' unrealistic negative feedback in the arctic. *Journal of Climate*, 22(17):4682–4695.

Brown, P. N. and A. C. Hindmarsh
1989. Reduced storage matrix methods in stiff ode systems. *J. Appl. Math. > Comp*, 31(11):40–91.

Budyko, M. I.
1969. The effect of solar radiation variations on the climate of the earth. *Tellus*, 21(5):611–619.

Budyko, M. I.
1972. The future climate. *Eos, Transactions American Geophysical Union*, 53(10):868–874.

Desbruyères, D. G., S. G. Purkey, E. L. McDonagh, G. C. Johnson, and B. A.

King
2016. Deep and abyssal ocean warming from 35 years of repeat hydrography. *Geophysical Research Letters*, 43(19):10,356–10,365. 2016GL070413.

Donohoe, A. and D. S. Battisti
2011. Atmospheric and surface contributions to planetary albedo. *Journal of Climate*, 24(16):4402–4418.

Eisenman, I.
2012. Factors controlling the bifurcation structure of sea ice retreat. *Journal of Geophysical Research: Atmospheres*, 117(D1). D01111.

Eisenman, I. and J. S. Wettlaufer
2009. Nonlinear threshold behavior during the loss of arctic sea ice. *Proceedings of the National Academy of Sciences*, 106(1):28–32.

Fetterer, F., K. Knowles, W. Meier, and M. Savoie
2016. Sea ice index, version 2. *Boulder, Colorado USA. NSIDC: National Snow and Ice Data Center.*

Flocco, D., D. L. Feltham, and A. K. Turner
2010. Incorporation of a physically based melt pond scheme into the sea ice component of a climate model. *Journal of Geophysical Research: Oceans*, 115(C8):n/a–n/a. C08012.

Fredriksen, H.-B. and M. Rypdal
2017. Long-range persistence in global surface temperature explained by linear multi-box energy balance models. *Submitted*.

Geoffroy, O., D. Saint-Martin, D. Olivié, A. Voldoire, G. Bellon, and S. Tytéca
2013. Transient climate response in a two-layer energy-balance model. part i: Analytical solution and parameter calibration using cmip5 aogcm experiments. *Journal of Climate*, 26(6):1841–1857.

Gyory, J., A. J. Mariano, and E. H. Ryan
2013. "the east greenland current." ocean surface currents. http://oceancurrents.rsmas.miami.edu/atlantic/east-greenland.html.

Hansen, J.
2007. Climate simulations for 1880-2003 with giss model. *Clim. Dym. 29, 661-696*.

Hansen, J.
2011. Earth's energy imbalance and implications. *Atmos Chem Phys, 11, 13421-13449*.

Held, I. M. and M. J. Suarez
1974. Simple albedo feedback models of the icecaps. *Tellus*, 26(6):613–629.

Hindmarsh, A. C.
1983. Odepack, a systematized collection of ode solvers," in scientific computing, r. s. stepleman et al. (eds.). *IMACS Transactions on Scientific Computation*, 1:55–64.

Hoffman, P. F., A. J. Kaufman, G. P. Halverson, and D. P. Schrag
1998. A neoproterozoic snowball earth. *Science*, 281(5381):1342–1346.

Huang, Y. and M. Bani Shahabadi
2014. Why logarithmic? a note on the dependence of radiative forcing on gas concentration. *Journal of Geophysical Research: Atmospheres*, 119(24):13,683–13,689. 2014JD022466.

IPCC
2013. Fifth assessment report, ar5.

Kaper, H. and H. Engler
2013. *Mathematics and Climate*.

Lenton, T. M.
2011. Early warning of climate tipping points. *Nature Clim. Change*, 1(4):201–209.

Lenton, T. M., H. Held, E. Kriegler, J. W. Hall, W. Lucht, S. Rahmstorf, and H. J. Schellnhuber
2008. Tipping elements in the earth's climate system. *Proceedings of the National Academy of Sciences*, 105(6):1786–1793.

Leppäranta, M.
1993. A review of analytical models of seaice growth. *Atmosphere-Ocean*, 31(1):123–138.

Lin, R. and G. North
1990. A study of abrupt climate change in a simple nonlinear climate model. *Climate Dyn. 4: 253.*

Lindsey, R.
2010. What if global warming isnt as severe as predicted? : Climate q and a : Blogs. earth observatory, part of the eos project science office, located at nasa goddard space flight center.

Marotzke, J. and P. M. Forster
2015. Forcing, feedback and internal variability in global temperature trends. *Nature*, 517:565–570.

Maykut, G. A. and M. G. McPhee
1995. Solar heating of the arctic mixed layer. *Journal of Geophysical Research: Oceans*, 100(C12):24691–24703.

Maykut, G. A. and N. Untersteiner
1971. Some results from a time-dependent thermodynamic model of sea ice. *Journal of Geophysical Research*, 76(6):1550–1575.

Mengel, J., A. Short, and G. North
1988. Seasonal snowline instability in an energy balance model. *Climate Dyn. 2: 127*.

Morice et al.
2012. Combined land [crutem4] and marine [sst anomalies from hadsst3] temperature anomalies on a 5 by 5 grid.

NASA/Operation IceBridge
2016. Front page image.

North, G.
1975a. Analytic solutions to a simple climate model with diffusive heat transport. *J. Atmos*.

North, G. R.
1975b. Theory of energy-balance climate models. *Journal of the Atmospheric Sciences*, 32(11):2033–2043.

North, G. R.
1984. The small ice cap instability in diffusive climate models. *Journal of the Atmospheric Sciences*, 41(23):3390–3395.

North, G. R., R. F. Cahalan, and J. A. Coakley
1981. Energy balance climate models. *Reviews of Geophysics*, 19(1):91–121.

North, G. R. and J. A. Coakley
1979. Differences between seasonal and mean annual energy balance model calculations of climate and climate sensitivity. *Journal of the Atmospheric Sciences*, 36(7):1189–1204.

Piron, M. A. C. and J. A. C. Pasalodos
2016. Nueva serie de extension del hielo marino artico en septiembre entre 1935 y 2014. *Revista de Climatologia Vol. 16: 1-19*.

Poulsen, C. J., R. T. Pierrehumbert, and R. L. Jacob
2001. Impact of ocean dynamics on the simulation of the neoproterozoic "snowball earth". *Geophysical Research Letters*, 28(8):1575–1578.

Rahmstorf, S.
2008. *Anthropogenic climate change: Revisiting the facts*, Pp. 34–53. Global warming: Looking beyond Kyoto.

R.Courant and D. Hilbert
1953. Methods of mathematical physics, vol. 1. *Interscience Publishers, Inc., New York, London*.

Reddy, S. M., S. J. Chary, A. Reddy, M. M. Reddy, M. M. Rao, and M. A. S. Chary
2003. *University Botany II : (Gymnosperms, Plant Anatomy, Genetics, Ecology)*. New Age International.

Rose, B. E. J. and J. Marshall
2009. Ocean heat transport, sea ice, and multiple climate states: Insights from energy balance models. *Journal of the Atmospheric Sciences*, 66(9):2828–2843.

Rypdal, K.
2017. Are simple climate models useful, and do they have to be derived from, or justified by, high-complexity models?

Scheffer, M., J. Bascompte, W. A. Brock, V. Brovkin, S. R. Carpenter, V. Dakos, H. Held, E. H. van Nes, M. Rietkerk, and G. Sugihara
2009. Early-warning signals for critical transitions. *Nature*, 461(7260):53–59.

Schweiger, A., R. Lindsay, J. Zhang, M. Steele, H. Stern, and R. Kwok
2011. Uncertainty in modeled arctic sea ice volume. *Journal of Geophysical Research: Oceans*, 116(C8):n/a–n/a. C00D06.

Sellers, W. D.

1969. A global climatic model based on the energy balance of the earth-atmosphere system. *Journal of Applied Meteorology*, 8(3):392–400.

Stefan, J.

1891. Ueber die theorie der eisbildung, insbesondere über die eisbildung im polarmeere. *Annalen der Physik*, 278(2):269–286.

Thomas, L.

1949. *Elliptic Problems in Linear Differential Equations over a Network, Watson Sci. Comput. Lab Report, Columbia University, New York.*

Thorndike, A. S.

1992. A toy model linking atmospheric thermal radiation and sea ice growth. *Journal of Geophysical Research: Oceans*, 97(C6):9401–9410.

Voigt, A. and D. S. Abbot

2012. Sea-ice dynamics strongly promote snowball earth initiation and destabilize tropical sea-ice margins. *Climate of the Past*, 8(6):2079–2092.

Wagner, T. J. W. and I. Eisenman

2015a. False alarms: How early warning signals falsely predict abrupt sea ice loss. *Geophysical Research Letters*, 42(23):10,333–10,341. 2015GL066297.

Wagner, T. J. W. and I. Eisenman

2015b. How climate model complexity influences sea ice stability. *Journal of Climate*, 28(10):3998–4014.

Winton, M.

2013. *Sea Ice–Albedo Feedback and Nonlinear Arctic Climate Change*, Pp. 111–131. American Geophysical Union.